Article

Current Biology

Diversity and sensorimotor specialization of head direction cells in the mouse thalamus

Graphical abstract

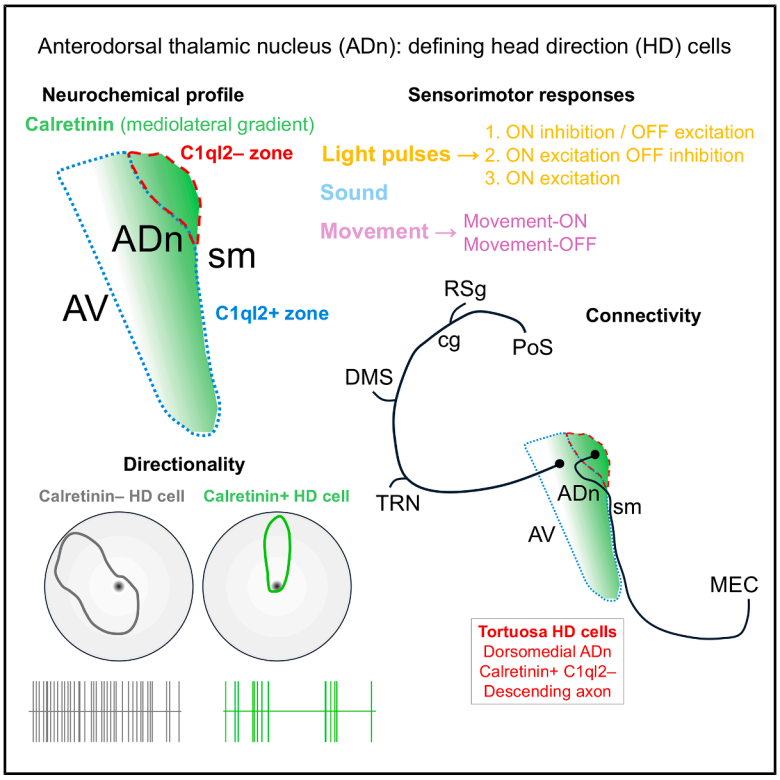

Highlights

- Calretinin distinguishes head direction cell subpopulations in the mouse thalamus
- Thalamic HD cells show distinct responses to light, sound, and movement
- Calretinin-positive cells project to deep layers of the entorhinal cortex
- HD cells are defined by combined activity, connectivity, and neurochemistry

Authors

Sara Hijazi, Shan Jiang, Mara S. Wülfing, Jacqueline Quach, Patrick A. Lachance, Michael E. Hasselmo, Tim J. Viney

Correspondence

tim.viney@pharm.ox.ac.uk

In brief

Hijazi and Jiang et al. identify distinct head direction (HD) cell subpopulations in the mouse anterodorsal thalamic nucleus, based on the combination of firing patterns, connectivity, and neurochemical profile, including calretinin immunoreactivity. Differential sensorimotor responses and projection targets suggest that HD cells integrate attention- and arousal-related information with directional signals.

Hijazi et al., 2026, Current Biology *36*, 1–17
June 22, 2026
https://doi.org/10.1016/j.cub.2026.05.026

CellPress

Please cite this article in press as: Hijazi et al., Diversity and sensorimotor specialization of head direction cells in the mouse thalamus, Current Biology (2026), https://doi.org/10.1016/j.cub.2026.05.026

Current Biology

CellPress
OPEN ACCESS

Article

Diversity and sensorimotor specialization of head direction cells in the mouse thalamus

Sara Hijazi,[1,3] Shan Jiang,[1,3] Mara S. Wülfing,[1] Jacqueline Quach,[1] Patrick A. Lachance,[2] Michael E. Hasselmo,[2] and Tim J. Viney[1,4,*]

[1]Department of Pharmacology, University of Oxford, Mansfield Road, Oxford OX1 3QT, UK
[2]Center for Systems Neuroscience, Boston University, 610 Commonwealth Avenue, Boston, MA 02215, USA
[3]These authors contributed equally
[4]Lead contact
*Correspondence: tim.viney@pharm.ox.ac.uk
https://doi.org/10.1016/j.cub.2026.05.026

SUMMARY

There is increasing recognition of diversity within functionally defined classes of spatially modulated brain cells. One such functional class, the head direction (HD) cells, provides our sense of direction and is essential for spatial navigation. HD signals are routed to the cortex via the thalamus, with the highest density of HD cells found within the anterodorsal thalamic nucleus (ADn). Variability in axonal projections and *in vivo* firing patterns suggest the existence of distinct neuronal subpopulations in the ADn. We investigated this diversity by extracellularly recording and juxtacellularly labeling single HD cells in subregions of the ADn in awake mice. We find that *in vivo* firing patterns of individual HD cells are differentially modulated by light pulses, sound, and movement, indicating sensorimotor specialization. We also reveal a mediolateral gradient of calretinin (CR)-expressing (CR+) cells, with CR+ HD cells having narrower tuning widths, lower peak firing rates, and different intrinsic properties compared with CR− HD cells. We identify distinct axonal projection patterns, including HD cells innervating the thalamic reticular nucleus (TRN) and different layers of the granular retrosplenial cortex, as well as HD cells with additional collaterals in the dorsomedial striatum. We also define an unusual CR+ subpopulation, the tortuosa HD cells, which possess twisted dendrites and a descending axon that does not innervate the TRN. Together, these findings suggest that ADn HD cells comprise specific cell types that integrate multimodal streams of sensorimotor input within their receptive fields that relate to attention and arousal, thereby providing downstream targets with dynamically updated and behaviorally relevant directional information.

INTRODUCTION

Spatial navigation is fundamental for survival. Head direction (HD) cells in the mammalian brain are required for spatial orientation, providing a dynamic representation of head position with respect to environmental (allocentric) and body-based (egocentric) cues.[1–3] In hippocampal and parahippocampal regions of the cerebral cortex, coordinated firing of HD cells with other spatially modulated neurons, including grid cells, border cells, and place cells, forms the cortical mnemonic system, which enables spatial navigation based on past experience stored in memory.[4–7] How is this cortical mnemonic system updated? The anterodorsal thalamic nucleus (ADn) contains a high density of HD cells, which receive sensorimotor messages primarily via the lateral mammillary nucleus.[1,8,9] The ADn is reciprocally connected to the granular retrosplenial cortex (RSg) and postsubiculum (dorsal presubiculum), and also projects to the entorhinal cortex (EC); all three cortical areas also contain HD cells.[10–18] The projections from the mouse ADn are not uniform, rather they comprise distinct medial and lateral subpopulations.[14] Ultimately, ADn directional and orientation signals are integrated with other spatial signals, updating the cortical mnemonic system.

Sensorimotor messages received by thalamic HD cells primarily comprise vestibular, proprioceptive, and visual signals.[1,19,20] Furthermore, thalamic HD cells can increase their firing rates in response to auditory cues, whisker stimulation, and social touch.[21] Restraining rats by hand can silence some thalamic HD cells but leave others unaffected.[8,22–24] Other sources, including the olfactory system[25] and cerebellum,[26] also modulate thalamic HD cell activity. The variety of messages integrated by the ADn raises the following hypotheses: (1) each HD cell receives the same range of inputs and has similar responses to particular sensorimotor inputs or (2) each HD cell receives different inputs and shows divergent responses. The second hypothesis is consistent with the notion of cell types. "Types" of ADn cells have been previously described, referring to differences in single parameters such as firing mode or synaptic target region. Here, we strictly define "cell type" as the *combination* of *in vivo* firing patterns, connectivity (especially axonal projection patterns), and neurochemical profile. We used single-neuron extracellular recordings followed by juxtacellular labeling to determine whether the ADn contains distinct cell types conveying a variety of sensorimotor messages reflecting attention and arousal.

Please cite this article in press as: Hijazi et al., Diversity and sensorimotor specialization of head direction cells in the mouse thalamus, Current Biology (2026), https://doi.org/10.1016/j.cub.2026.05.026

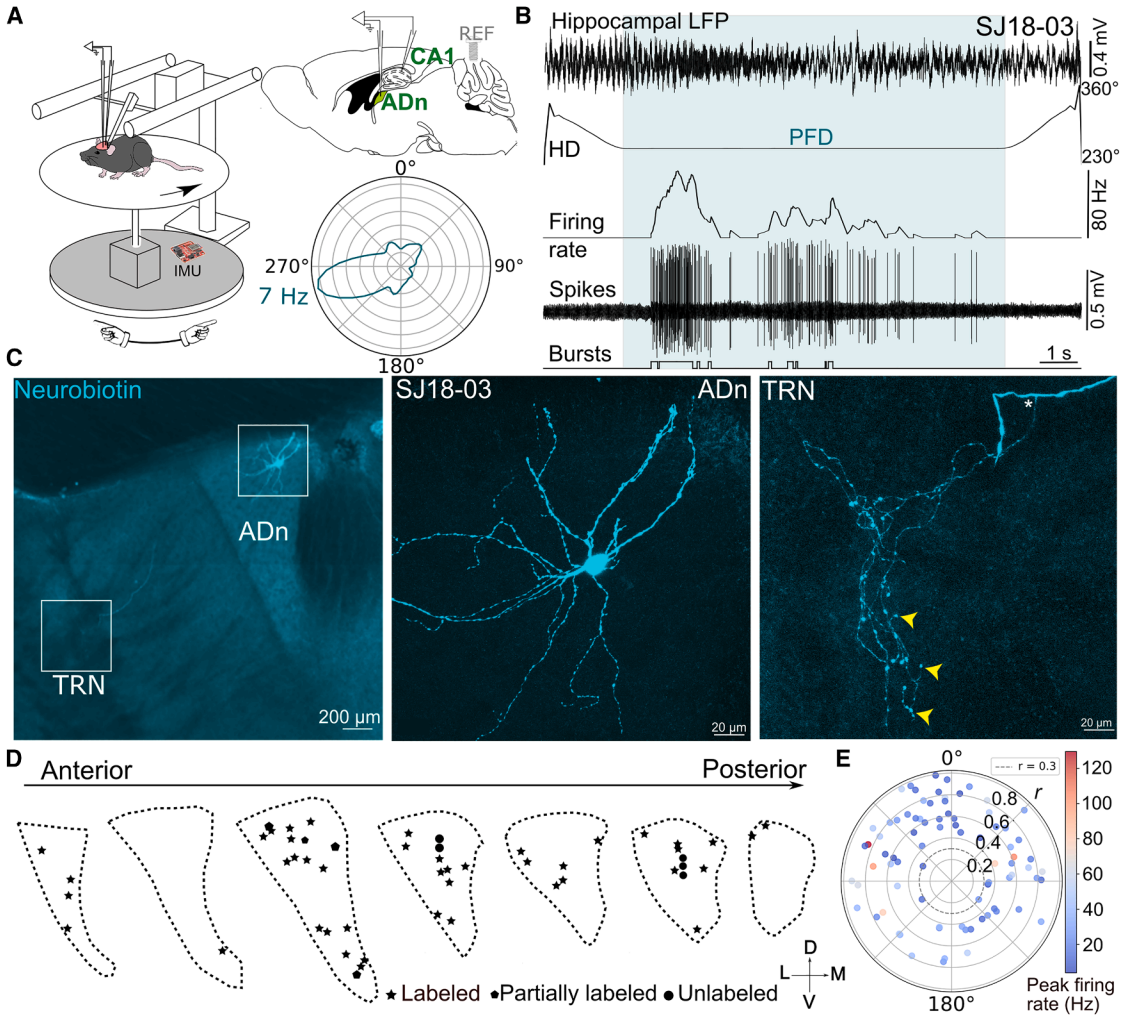

Figure 1. Distribution of single extracellularly recorded ADn HD cells

(A) Left, schematic of *in vivo* extracellular recordings in head-restrained mice. The turntable (gray) is passively rotated. An inertial measurement unit (IMU) is used to compute the turning angle. Top right, schematic sagittal brain section indicating target locations of glass electrodes. REF, electrical reference screw above the cerebellum. Bottom right, polar plot of the tuning curve from a recorded ADn HD cell (cell SJ18-03) with its peak firing rate indicated.

(B) Example simultaneous recordings of the hippocampal CA1 local field potential (LFP), HD, firing rate (bin size = 0.2 s), spikes, and spike bursts of the HD cell (SJ18-03). The shaded area marks the PFD.

(C) Left, epifluorescence micrograph of a coronal brain section showing the juxtacellularly neurobiotin-labeled HD cell (cyan, SJ18-03). Middle and right, confocal images (78.3 and 74.7 µm thick maximum intensity z-projections), showing the soma, partial dendrites, and axon terminals (e.g., arrowheads). Asterisk, main projection axon in the TRN and the origin of the collateral. Scale bars: left, 200 µm; middle and right, 20 µm.

(D) Schematic of different anteroposterior levels of the ADn, showing locations of recorded cells (stars, 44 labeled cells; pentagons, 4 partially labeled cells; circles, 6 unlabeled cells). Bregma from left to right (mm): −0.545, −0.62, −0.67, −0.72, −0.77, −0.845, and −0.895. See also Figure S1 for cell names and representative images.

(E) Polar plot demonstrating the features (mean vector length, PFD, and peak firing rate) of the recorded cells. Radial axis, mean vector length (*r*); PFD (angle); peak firing rate (color bar, Hz).

See also Figures S1 and S2 and Table S1.

RESULTS

Identification of HD cells in the mouse ADn

To extracellularly record and label single HD cells in the ADn, we passively rotated awake head-fixed mice while they spontaneously ran or rested on a running disc (Figure 1A).[27] We lowered a glass electrode into the thalamus to detect spiking activity, then manually rotated the recording apparatus so that the mouse's head rotated relative to the fixed visual features of the recording room (average rotation speed: 0.67°/s). HD cells were identified by an abrupt increase in firing in a specific direction; the HD at which they fired maximally defined the preferred firing direction (PFD) (Figures 1A, 1B, and S2A; Table S1).

After recording individual HD cells at different depths and mediolateral positions in the anterior thalamus, we juxtacellularly labeled one HD cell with neurobiotin in one or both hemispheres

Please cite this article in press as: Hijazi et al., Diversity and sensorimotor specialization of head direction cells in the mouse thalamus, Current Biology (2026), https://doi.org/10.1016/j.cub.2026.05.026

CellPress
OPEN ACCESS

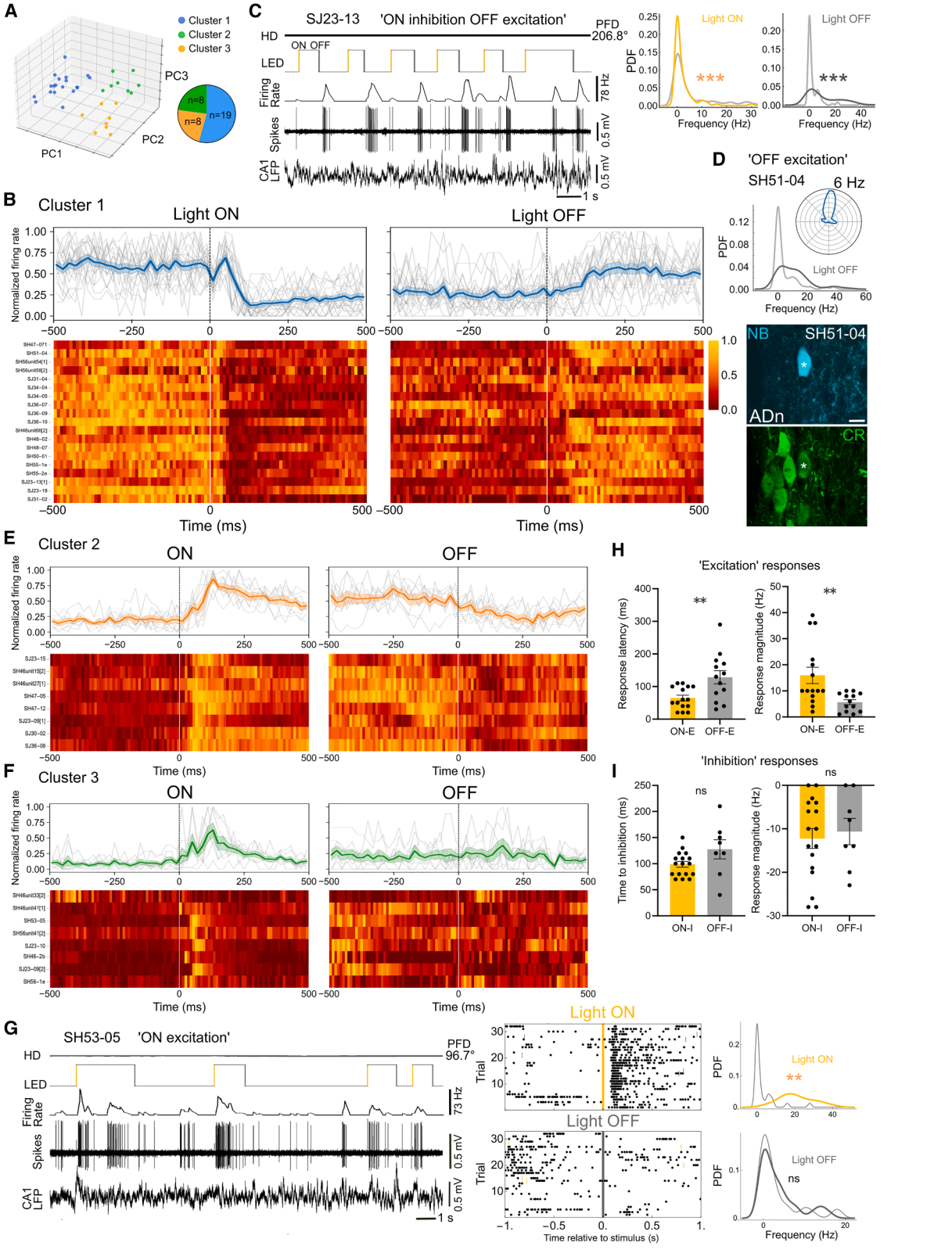

(legend on next page)

Please cite this article in press as: Hijazi et al., Diversity and sensorimotor specialization of head direction cells in the mouse thalamus, Current Biology (2026), https://doi.org/10.1016/j.cub.2026.05.026

for *post hoc* recovery (Figures 1C, 1D, and S1). We report 120 HD cells (including 2 bidirectional HD cells) and 3 non-HD cells localized to the ADn (Figures 1D, 1E, S1, and S2G; Table S1), covering the full directional range (Figures 1E, S2A, and S2C). For unidirectional HD cells, the peak firing rate was 23.7 [11.8–42.2] Hz (median [interquartile range, IQR]), and the background firing rate (i.e., outside the PFD) was 0.78 [0.3–1.7] Hz (Figures 1E, S2A, S2E, and S2F). The directional tuning width was 103.1 [48.1–180]°, and directional information content (how much HD information is conveyed by each spike) was 0.78 [0.53–1.13] bits/spike (Figures S2D and S2H). The sparsity (the proportion of the tuning curve to which the cell is responsive) was 0.47 [0.34–0.6], and directional coherence (a measure of the smoothness of the HD tuning curve) was 0.75 [0.54–0.87] (Figures S2I and S2J). These values are broadly similar to those of HD cells previously recorded in both head-restrained[21] and freely moving rodents.[3,8,28] In addition, we observed burst firing within the PFDs (Figures S2B and S2K–S2O).[20,27]

ADn HD cells differentially respond to light pulses

Given that rodent HD cell activity can be modulated by visual cues,[29,30] we tested whether mouse ADn HD cells responded to pulses of bright light. We observed a striking diversity of light responses for both single-neuron recordings (n = 27/34 tested cells, glass electrodes; n = 14 mice) and simultaneously recorded units (n = 8/12 tested units, silicon probes; n = 2 mice) (Figure 2; Table S2). A minority of tested cells were unresponsive to light pulses (n = 12/46 cells and units). To categorize the light-responsive cells, we performed principal-component analysis (PCA) followed by k-means clustering on normalized firing rates and identified 3 clusters (silhouette score 0.47; Figure 2A; Table S2).

Cluster 1 included HD cells that significantly decreased firing at light ON and/or significantly increased firing at light OFF (“ON inhibition/OFF excitation”; $p < 0.05$, Wilcoxon signed-rank tests, n = 9/19; Figures 2B–2D; Table S2). Cluster 2 contained cells that showed a sustained increase in firing at light ON, followed by decreased firing at light OFF (“ON excitation/OFF inhibition”; $p < 0.05$, n = 7/8; Figure 2E; Table S2). Cluster 3 predominantly contained cells that showed a transient increase in firing at light ON (“ON excitation”; $p < 0.05$, n = 7/8; Figures 2F and 2G). Importantly, simultaneously recorded units (which included some units within and some outside their PFDs) showed different light-response profiles, and one HD cell responded similarly both within and outside its PFD (SJ23-09; Table S2), suggesting segregated inputs.

We also observed differences in response latencies. ON excitation responses were significantly faster than OFF excitation (64.7 ± 8.8 vs. 128.5 ± 20.3 ms, unpaired t test, $t_{(26)}$ = 3.021, $^{*}p$ = 0.0056; n = 15 cells and units for ON excitation, n = 13 for OFF excitation; Figure 2H). ON excitation also had a larger response magnitude than OFF excitation (10 [8–22] vs. 6 [2–9] Hz, Mann-Whitney test, $^{**}p$ = 0.0025; Figure 2H). In contrast, ON inhibition was similar to OFF inhibition both in terms of latency (98.8 ± 5.7 vs. 127.5 ± 18.2 ms, unpaired t test, $t_{(23)}$ = 1.94, p = 0.065; n = 17 ON inhibition, n = 8 OFF inhibition; Figure 2I) and magnitude (−12.2 ± 2.3 vs. −10.6 ± 3 Hz, p = 0.76, Mann-Whitney test; Figure 2I). Latencies were in a similar range to those reported for rat ADn HD cells following the presentation of cue cards.[29] These data demonstrate the existence of subpopulations of mouse HD cells with different responses to pulses of light.

Sound and movement sensitivity of ADn HD cells

Some HD cells increase their activity in response to “clicks.”[21] We confirmed this by presenting “click” auditory stimuli to 26 HD cells from 10 mice (Figure 3; Table S3). We observed an abrupt increase in firing after the stimulus (15 [10.5–29] ms latency, 23.6 ± 4.2 Hz response magnitude; n = 14 cells, recorded in the PFD); 5 of these sound-activated cells exhibited elevated firing for at least 0.5 s after the stimulus (Figures 3A–3C) and 1 cell decreased firing (Figures 3D and 3E). The remaining tested cells were unresponsive within their PFD (n = 8/26). Interestingly, sound-responsive HD cells became unresponsive outside their PFDs (Table S3), suggesting that the cell must be sufficiently depolarized to enable a response.

We observed that mice twitched in response to some (but not all) click stimuli (“acoustic-startle response,” related to the reflex described by Yeomans et al.[31]). To test whether cells responded to the sound itself or were only evoked by the twitches, we

Figure 2. Differential responses of ADn HD cells to light pulses

(A) Left, three-dimensional scatterplots using the three best PCA components (k = 3), color coded by cluster. Right, pie chart displaying the number of cells and units in each cluster.

(B, E, and F) Top, cluster-averaged peri-stimulus time histograms aligned to light ON or OFF. Normalized firing rates (20-ms time bins) within a −500- to +500-ms window relative to light pulse onset or offset (time 0; dashed vertical lines). Thin gray traces represent individual cells or units, colored lines indicate the cluster mean, and shaded regions denote ±SEM. Bottom, heatmap of responses of individual HD cells and units from each cluster. Firing rate (bin size, 20 ms) is normalized per row (cf. calibration bar). Cell name followed by [1] indicates data from the PFD only; [2] indicates data from the unpreferred direction (UPFD) only.

(C) Left, an HD cell reduced its firing rate at light ON and increased firing at light OFF (ON inhibition/OFF excitation, cell SJ23-13). Top to bottom: HD (maintained in its PFD), light pulse (orange, light onset [ON]; dark gray, light offset [OFF]), mean firing rate (bin size = 0.2 s), spikes, hippocampal CA1 LFP. Right, probability density functions (PDFs) of firing rates 0.5 s before (light gray) vs. 0.5 s after light ON (orange) or OFF (dark gray). $^{***}p < 0.001$.

(D) Top, PDF of a juxtacellularly labeled HD cell (SH51-04), showing an increase in firing after light OFF (OFF excitation). Inset, polar plot of the HD tuning; peak firing rate of 6 Hz (radial axis). Bottom, confocal images (1.7 μm thick maximum-intensity z-projection) of the HD cell (SH51-04, asterisk; neurobiotin, NB, cyan) that was immunopositive for CR (green). Scale bar, 10 μm.

(G) Left, an HD cell showing an abrupt and transient increase in firing at light ON but not at light OFF (ON excitation, cell SH53-05). Middle, raster plots of responses of SH53-05. Each point represents a spike. Dark gray and orange ticks inside the raster plots represent other light OFF and ON events, respectively. Note consistent latencies for light-ON responses. Right, PDFs of firing rates for cell SH53-05 after light ON or light OFF. $^{**}p < 0.01$; ns, not significant.

(H and I) Response latency and magnitude after light ON (orange) or light OFF (gray) for excitation responses and inhibition responses; data presented as mean ± SEM. $^{**}p < 0.01$; ns, not significant.

See also Table S2.

Please cite this article in press as: Hijazi et al., Diversity and sensorimotor specialization of head direction cells in the mouse thalamus, Current Biology (2026), https://doi.org/10.1016/j.cub.2026.05.026

CellPress
OPEN ACCESS

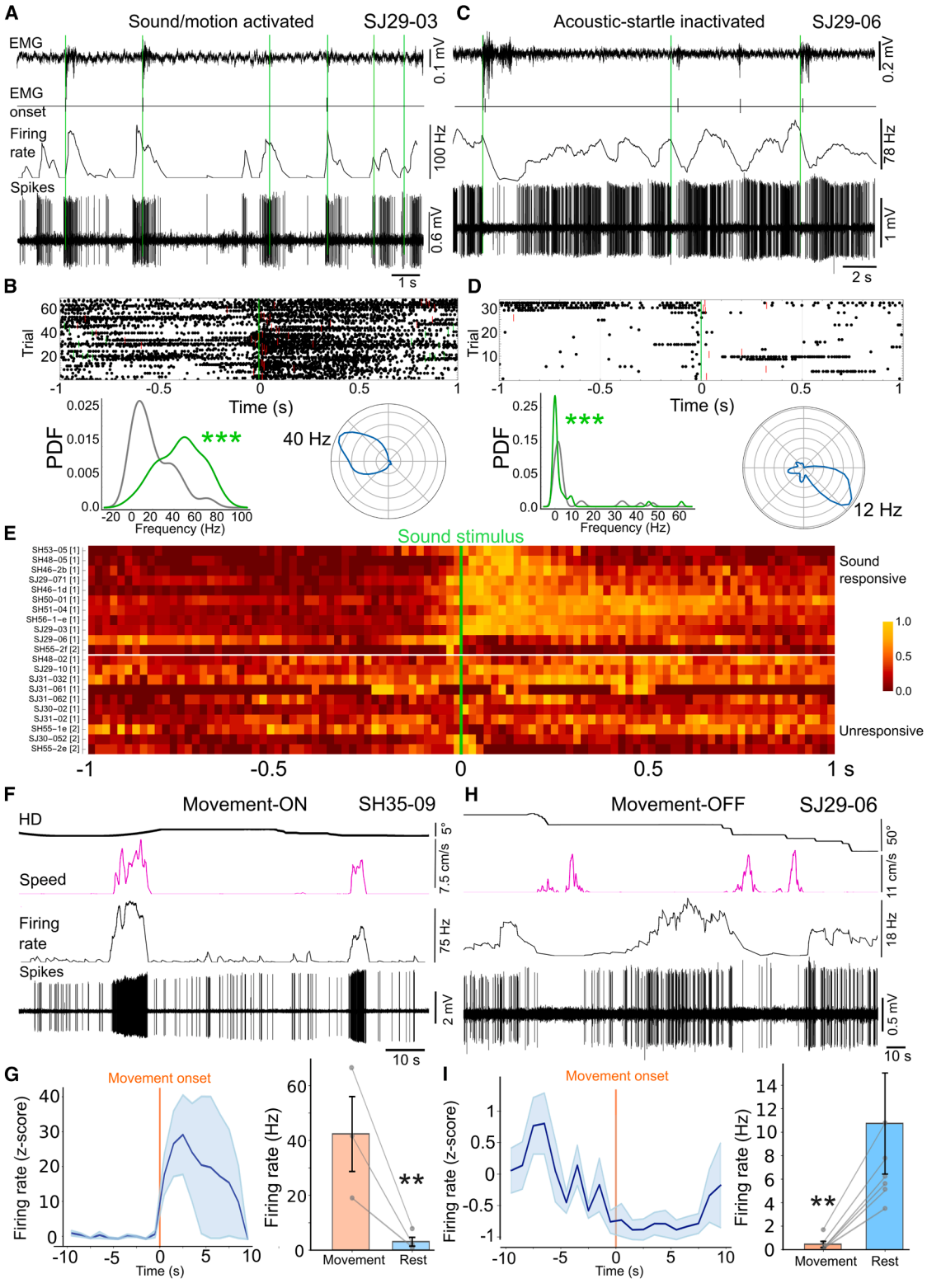

Figure 3. Responses of ADn HD cells to sound and body movement

(A) An HD cell showing an abrupt and transient increase in firing at sound onset (sound activated, cell SJ29-03). These trials occurred while the animal was resting (running speed = 0), and the cell was in its PFD. Click sound stimuli are indicated with green bars. Top to bottom: electromyography (EMG) trace, detected evoked EMG responses, firing rate (bin width = 0.2 s), and spikes.

(legend continued on next page)

Please cite this article in press as: Hijazi et al., Diversity and sensorimotor specialization of head direction cells in the mouse thalamus, Current Biology (2026), https://doi.org/10.1016/j.cub.2026.05.026

additionally recorded neck muscle signals for a subset of recordings. We observed that firing rates significantly increased on trials with and without twitches (Figures 3B–3E and S3A). We also observed HD cells that *only* responded when click stimuli were followed by twitches, which either induced a decrease in firing (acoustic-startle inactivated; Figures 3D, 3E, and S3B) or an increase in firing (acoustic-startle activated; Figure S3C). In addition to twitch-modulated activity, we observed HD cells that consistently fired at high rates when the mouse was running (n = 11/16 movement-ON HD cells; Figures 3F and 3G). Other cells abruptly stopped firing during running periods (n = 5/16 movement-OFF HD cells; Figures 3H and 3I).

Finally, we analyzed whether individual HD cells responded similarly to light pulses, sound, and movement. The majority of tested cells were multimodal (n = 13/22 cells; Tables S2 and S3). For example, cell SH50-01 increased firing following the sound stimulus but decreased firing in response to light pulses. Overall, these data demonstrate that ADn HD cells show differential, multimodal responses to light, sound, and movement.

CR forms a mediolateral gradient in the ADn

To further define the recorded HD cells, we tested the juxtacellularly labeled cells for neurochemical markers. We found that ~30% of HD cells were immunopositive for calretinin (CR) (CR+, n = 13/42 tested cells; Figure 4; Table S1). *Calb2*-expressing cells (for CR) have previously been excluded from the ADn due to high *Calb2* expression levels in adjacent thalamic nuclei.[32] However, using streptavidin to delineate the ADn (recognizing the high levels and density of biotin), we detected CR+ neurons that were clearly within the medial ADn, adjacent to the stria medullaris, forming a mediolateral gradient (Figures 4A–4C, S4, and S5). Weakly CR+ neurons were intermingled with those lacking detectable immunoreactivity (CR−), with the highest density of CR− neurons adjacent to the anteroventral nucleus (AV) and laterodorsal nucleus (LD) (Figures 4A–4C, S4, and S5). The medial band of CR+ cells extended ventrally into the interanterodorsal thalamus (Figure S4D). We found that ~30% of ADn cells were CR+ (122 ± 23 CR+ cells/472 ± 103 DAPI nuclei from n = 3 mice), similar to the proportion of tested juxtacellularly labeled HD cells. The centrolateral and paraventricular thalamic nuclei also contained CR+ cells, as did the LD (Figures S4 and S5).[33] Similar to the lateral ADn, the AV lacked CR immunoreactivity (Figures 4A and S4B). However, unlike the ADn, the AV exhibited a mediolateral gradient of Purkinje cell protein 4 (PCP4) immunoreactivity (Figure S4C).

CR distinguishes two subpopulations of ADn cells

Next, we tested whether CR was associated with any differences in firing patterns. We found that CR+ cells had significantly lower peak firing rates (7.0 [3.6–16.8] Hz for n = 8 CR+ HD cells vs. 28.7 [9.8–50.9] Hz for n = 25 CR− HD cells; Mann-Whitney test, $^*p$ = 0.031; Figure 4E; Table S4) and narrower tuning widths (57.9° ± 11.5° [CR+] vs. 129.6° ± 14.6° [CR−], unpaired t test, $t_{(31)}$ = 2.663, $^*p$ = 0.012; Figure 4F; Table S4). Two representative cells are shown in Figures 4G and 4H. Interestingly, only 1 of 7 labeled light-responsive cells was CR+ (Figure 2D; Table S2).

To gain insight into why CR+ HD cells had narrower tuning widths and lower firing rates *in vivo*, we examined their intrinsic properties *ex vivo* using whole-cell patch-clamp recordings. We sampled cells in different locations of the ADn to match the *in vivo* locations and recorded 34 cells, of which 8 were CR+ (23.5%) and 22 were CR− (64.7%; the remaining recorded ADn cells were not recovered; Figures 4I and S6A). Cells were clamped at their resting membrane potential and increasing currents were injected to quantify both passive and active properties (Figures 4J–4L and S6). ADn cells exhibited a rebound burst following a hyperpolarizing current injection of 500 ms duration (n = 19/20 cells; Figures 4J and S6B). When the duration of current injection was decreased to 100 ms, the number of action potentials (APs) fired during the burst was reduced; we observed a significant decrease in the number of APs firing within a burst in CR+ cells compared with CR− cells (0.2 ± 0.2 [n = 5 CR+ cells] vs. 2.0 ± 0.4 [n = 13 CR− cells] APs from 6 mice, Mann-Whitney test, $^*p$ = 0.010; Figures 4J and S6B). The resting membrane potential, sag potential, and input resistance were similar for CR+ and CR− neurons (n = 8 CR+ and n = 22 CR− cells from 8 mice; Figures S6C–S6E; Table S4).

Next, we examined active properties and found that CR+ neurons had a broader AP width (0.701 ± 0.05 [CR+] vs. 0.530 ± 0.04 [CR−], t test, $t_{(32)}$ = 2.495, p = 0.0293; Figure 4K). The AP threshold, rheobase, AP amplitude, and afterhyperpolarization (AHP) potential were similar across groups (Figures S6F–S6I). Interestingly, we observed that CR+ neurons had a lower firing rate with increasing current injections (two-way repeated measures ANOVA (group × current effect), $F_{10,259}$ = 1.893, $^*p$ = 0.046; Figure 4L), as well as a lower maximum firing frequency (96.3 ± 12.7 [CR+] vs. 130.0 ± 8.2 [CR−], t test, $t_{(26)}$ = 2.177,

(B) Top, raster plot of responses of the cell in (A). Each point is a spike. Green ticks, other sound onset events; red ticks, evoked EMG onset times. Bottom left, PDFs of firing rates 0.5 s before (gray) and 0.5 s after (green) sound onset. Bottom right, polar plot of the HD tuning curve with its peak firing rate.
(C) An HD cell that reduced its firing rate following the sound stimulus coincident with evoked EMG activity (acoustic-startle inactivated, cell SJ29-06); firing rate bin width = 1 s.
(D) Raster plot, PDFs, and polar plot with its peak firing rate for the cell in (C).
(E) Heatmap of responses of all tested HD cells to sound. Bin width, 20 ms. Firing rates are normalized per row (color bar). Categories: sound activated (n = 4), sound activated sustained (n = 5), sound inactivated (n = 2), and unresponsive (n = 10). (1) Recorded only in the PFD or (2) only in the UPFD.
(F) A movement-ON HD cell (SH35-09), showing a large increase in firing specifically during running within its receptive field. From top to bottom: mouse HD, mouse running speed, FR (bin size = 1 s), spike trace.
(G) Left, Z scored firing rate of the HD cell in (F) (normalized based on average firing rate 10 s before movement onset), aligned to the onset of movement (10 s before and after; 1-s time bins). Shaded area indicates ± SEM. Right, bar chart of firing rate during movement and rest (paired data).
(H) A movement-OFF HD cell (SJ29-06). Note suppression of firing during running within its receptive field. Firing rate bin width = 10 s.
(I) Z scored firing rate and bar chart for the cell in (H). $^{***}p < 0.001$; $^{**}p < 0.01$.
See also Figure S3 and Table S3.

Please cite this article in press as: Hijazi et al., Diversity and sensorimotor specialization of head direction cells in the mouse thalamus, Current Biology (2026), https://doi.org/10.1016/j.cub.2026.05.026

CellPress
OPEN ACCESS

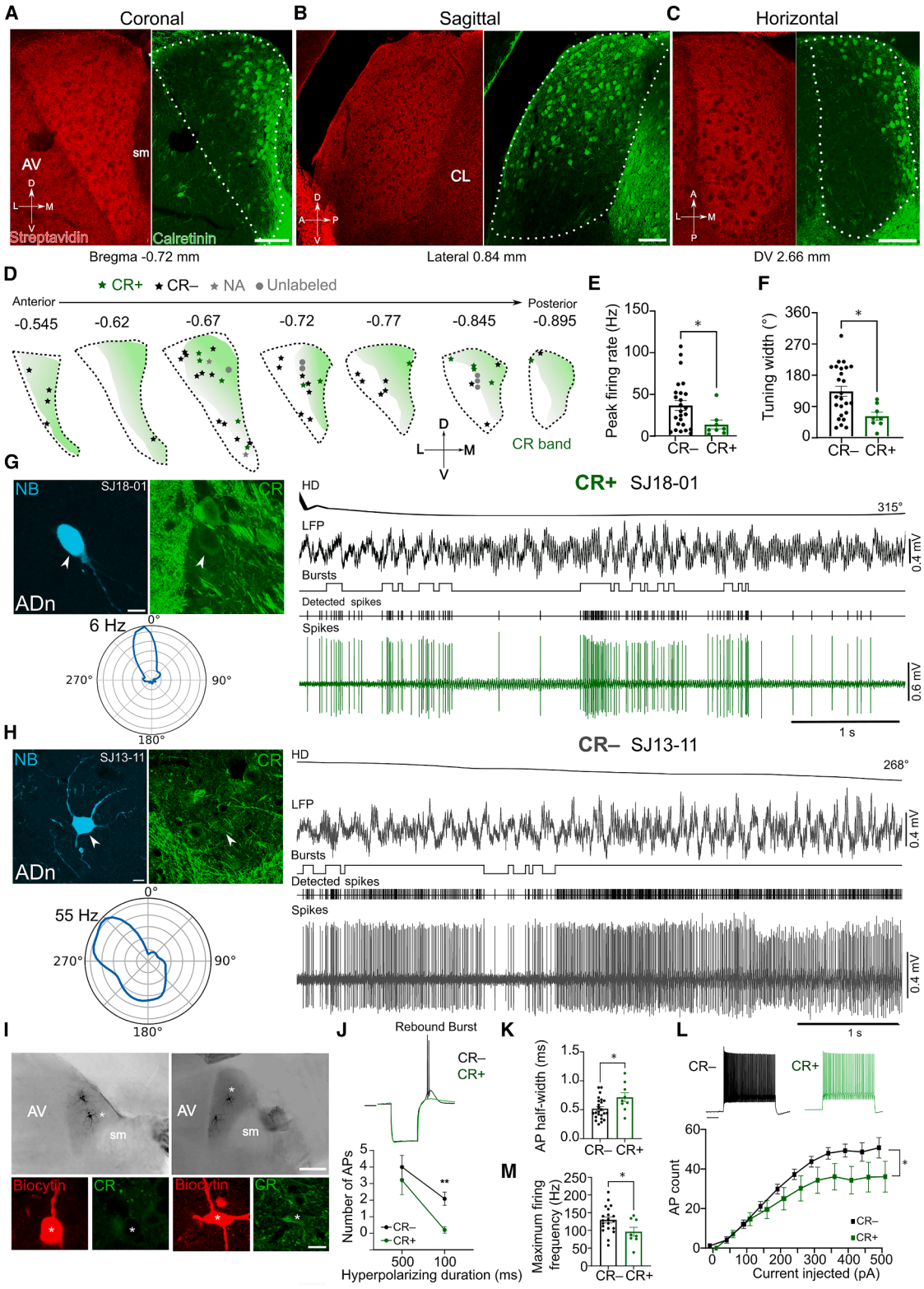

Figure 4. Comparisons of CR+ and CR– ADn cells

(A–C) The mouse ADn (dashed area) visualized by streptavidin (for biotin, red) at three different orientations. Note the mediolateral gradient for CR. Confocal single optical sections. Scale bars, 100 μm. Abbreviations: D, dorsal; L, lateral; M, medial; V, ventral; A, anterior; P, posterior; DV, dorsoventral position from the brain surface; AV, anteroventral nucleus; sm, stria medullaris; CL, centrolateral nucleus.

(legend continued on next page)

Please cite this article in press as: Hijazi et al., Diversity and sensorimotor specialization of head direction cells in the mouse thalamus, Current Biology (2026), https://doi.org/10.1016/j.cub.2026.05.026

*p = 0.038; Figure 4M), consistent with the *in vivo* firing pattern differences. These *in vivo* and *ex vivo* data show that CR distinguishes two distinct subpopulations of ADn cells.

Connectivity of ADn CR+ and CR– HD cells

To make predictions about how the differences in firing patterns might affect their postsynaptic targets, we examined the connectivity of mouse CR+ and CR− ADn neurons. We observed diversity in axonal projections, based on anterograde and retrograde viral tracing and by following axons of juxtacellulary labeled HD cells (Figures 5, 6, and 7). Complement C1q-like 2 (C1ql2) has been described as a selective and conserved marker of the ADn.[34] We first injected the retrosplenial cortex of C1ql2-Cre mice with a Cre-dependent retrograde adeno-associated virus (AAV), and observed retrogradely labeled cells in the majority of the ADn but limited labeling in the medial CR+ band (Figures 5A and 5B). Only 7.5% of GFP+ cells were CR+ (n = 2 sections from 2 mice; Figure 5C). After injecting a retrograde tracer into deep layers of the caudal medial EC (MEC; Figure 5D), we observed retrogradely labeled cells in the medial ADn (Figure 5E). The distribution strongly overlapped with CR (74% CR+, n = 81/109 retrogradely labeled GFP+ cells from n = 3 mice; Figure 5F). In contrast to the GFP+ cells projecting to the retrosplenial cortex, which had axons projecting across the AV (Figure 5B), MEC-projecting ADn cells had axons traveling ventrally, away from the thalamic reticular nucleus (TRN) (Figure 5E).

Immunolabeling for CR revealed that the ADn comprises four molecularly distinct subpopulations: C1ql2+/CR− (59%), C1ql2−/CR+ (12%), C1ql2+/CR+ (23%), and C1ql2−/CR− (5%) (Figures 5G and 5H). Notably, the C1ql2− subpopulation was localized to the dorsomedial ADn. To confirm that a subpopulation of CR+ cells in the medial ADn lack C1ql2, we injected a Cre-dependent dual reporter AAV into the ADn of C1ql2-Cre mice. This enabled simultaneous visualization of C1ql2+ (Cre-ON, GFP+; ∼80%) and C1ql2− (Cre-OFF, dTomato+; ∼20%) neurons (Figures 5I and 5J). We also injected another batch of C1ql2-Cre mice with a mixture of Cre-ON (GFP) and Cre-OFF (mRuby) AAVs and confirmed this observation (Figure 5I). These data reveal a subpopulation of medial CR+ ADn cells that mainly lack C1ql2 and preferentially project to the MEC, and a larger subpopulation of lateral (mainly CR−) ADn cells projecting to more dorsocaudal cortical areas, including the retrosplenial cortex, consistent with a recent report.[14]

Next, we examined labeled ADn HD cells by following their axons and identifying collaterals (n = 13/44 labeled cells; Table S1). Most labeled HD cells were distributed in the middle and lateral regions of the ADn and, consistent with the tracing data, axons followed a typical route via the TRN, internal capsule, dorsomedial striatum (DMS), and cingulum bundle (n = 8/13 cells; Figures 1C, 1D, 6C, 6D, 6H, 7B, and S1A; Table S1).[27] A representative CR− cell (SJ19-02) from the lateral ADn (Figures 6B–6D and S1A) had a high peak firing rate (61 Hz) and high mean vector length (r = 0.84; Figure 6A; Table S1). Some of its distal dendritic tips extended across the border of the ADn into the internal medullary lamina (Figure 6C). The axon emerged from the medial side of the soma and formed a hairpin turn. It looped back across the soma toward the lateral border, then crossed the AV to reach the TRN, where it gave rise to a total of 5 collaterals at two distinct sites within the TRN, forming terminals (n = 109 large terminals observed; Figures 6E–6G). Terminals of SJ19-02 and another CR− HD cell (SJ18-03) were double immunopositive for vGLUT1 and vGLUT2 (Figures 1C and 6F).

The main axon of cell SJ19-02 continued rostrally via the internal capsule and DMS; no collaterals were observed (Figure 6D). The axon traversed the corpus callosum and entered the cingulum bundle. At the level of the triangular septal nucleus (∼0.35 mm posterior to bregma), the axon turned and headed caudally within the medial part of the cingulum. The main axon formed a collateral at the level of the dorsal hippocampus (∼1.35 mm posterior to bregma) and innervated the RSg. Terminals were observed in layers 1, 2, and 3 (Figure 6H). The main axon continued caudally and was last observed branching from the cingulum into the deep layers of the postsubiculum (∼4.2 mm posterior to bregma). We identified 3 other CR− HD cells that followed the same trajectory but formed additional collaterals in the DMS (SJ13-11, SJ09-06, SH79-07; Figures 7A–7E and S1; Table S1). A collateral of HD cell SH79-07 gave rise to terminals that innervated cholinergic neurons in the DMS (Figure 7E). The main axon continued into the cingulum bundle and branched extensively in the RSg (Figure 7B) and postsubiculum, where it formed terminals (last observed in the most dorsal part of postsubiculum ∼4 mm from bregma).

(D) Schematic showing locations of identified ADn cells, along with their CR immunoreactivity. Shaded areas indicate the CR zone. NA, CR immunoreactivity not available.
(E and F) CR+ cells showed lower peak firing rates and narrower tuning widths compared with cells lacking CR immunoreactivity (CR−).
(G) Left, a labeled CR+ HD cell (SJ18-01) in the ADn (arrowhead). Confocal maximum-intensity z-projection (3.5 μm thick); neurobiotin (NB, cyan); CR (green). Scale bar, 10 μm. Below, polar plots of the HD tuning curve with peak firing rates indicated. Right, firing patterns within the PFD. Top to bottom: HD angle, hippocampal CA1 LFP showing transient theta oscillations, detected bursts, detected spikes, and spikes. Note 50 Hz electrical noise present in the LFP.
(H) Same as in (G) but for a CR− HD cell (SJ13-11). The confocal z-projection is 12.9 μm thick.
(I) Examples of biocytin-labeled ADn cells recorded *ex vivo*. Left, the cell denoted by the asterisk was tested for CR (green, inset) and was CR−. Right, a CR+ cell. Biocytin, black (main images), red (insets). Scale bar: 100 μm, inset 5 μm.
(J) Top, representative traces of voltage responses following a 100-ms hyperpolarizing step (−250 pA) from a CR− (black) and a CR+ (green) cell, illustrating the lack of rebound bursting in CR+ cells. Scale bar: 50 ms. Bottom, paired comparison of the mean (±SEM) number of APs within a burst at two different durations of current injection (n = 13 CR− and n = 7 CR+ cells from 8 mice). **p < 0.01.
(K) AP half-width in ms (n = 22 CR− and n = 8 CR+ cells from 8 mice).
(L) Top, representative traces of voltage responses following a depolarizing step (+500 pA) from CR− (black) and CR+ (green) cells, illustrating the decreased firing frequency in CR+ cells. Scale bar: 100 ms. Bottom, average AP frequency in response to 0–500 pA current steps, illustrating a significant decrease in firing frequency in CR+ cells at high-current injections. *p < 0.05.
(M) The average maximum firing frequency of CR− and CR+ cells (n = 13 CR− and n = 7 CR+ cells from 8 mice). *p < 0.05.
See also Figures S4–S6 and Table S4.

Please cite this article in press as: Hijazi et al., Diversity and sensorimotor specialization of head direction cells in the mouse thalamus, Current Biology (2026), https://doi.org/10.1016/j.cub.2026.05.026

CellPress
OPEN ACCESS

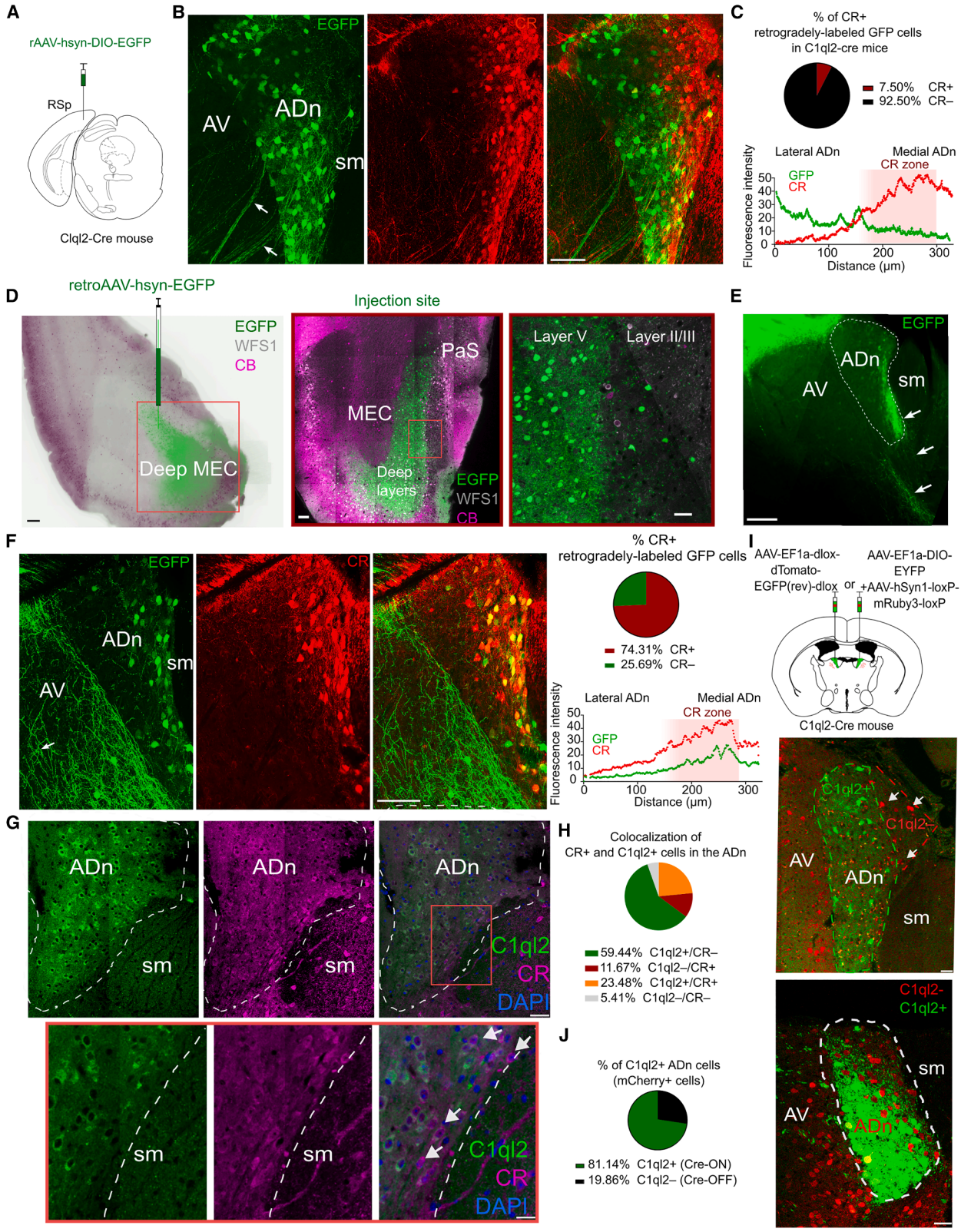

(legend on next page)

Please cite this article in press as: Hijazi et al., Diversity and sensorimotor specialization of head direction cells in the mouse thalamus, Current Biology (2026), https://doi.org/10.1016/j.cub.2026.05.026

We also recorded and labeled two unusual cells in the dorsomedial region of the ADn (TV188-06 and SJ19-04; Figures 7F–7M). Both cells were CR+ (Figures 7G and 7L) and fired in bursts within their PFDs (Figures 7F and 7K; Table S1). Cell SJ19-04 showed typical CR+ HD tuning, with a low peak firing rate (1 Hz) and a narrow tuning width (7.8°; Figure 7K). The contorted dendrites resembled the twisting, flowing branches of *Salix babylonica* var. *pekinensis "Tortuosa"* (corkscrew willow tree) (Figures 7H and 7J). The axons of both cells headed ventrally from the ADn and we did not observe any collaterals heading toward the TRN, despite using sensitive diaminobenzidine reactions to visualize and follow the axon (Figures 7I, 7J, and 7M). The axon of TV188-06 emerged from the ventral part of the soma and initially headed laterally across the ADn in the direction of the TRN. However, compared with the majority of HD cells (e.g., Figures 1C, 6C, 6D, and 7B), the axon sharply looped back over itself and headed ventrally, to leave the ADn alongside the stria medullaris (Figures 7I and 7J). The axon traveled in an anteroventral direction along the edge of the stria medullaris and headed laterally until ~−0.10 mm posterior to bregma, where it began to head in a lateroposterior direction, traveling ventral of the posterior part of the anterior commissure. It was last observed within the endopiriform cortex (~0.34 mm posterior to bregma), still heading posteriorly (Figure 7I). We name these ADn cells "tortuosa HD cells," based on their twisted dendrites, descending axons, lack of TRN collaterals, dorsomedial, molecular profile (CR+/C1ql2−), and HD activity (Figures 7F–7M), supported by the tracing data (Figure 5).

DISCUSSION

Glass electrode extracellular recordings in the ADn of awake head-fixed mice during passive rotation provided us with reliable measures of HD cell activity that were similar to freely moving conditions.[28] Juxtacellular labeling of recorded cells enabled us to recognize diversity based on the *combination* of properties, including neuronal activity, neurochemical profile, and axonal projections, rather than relying on single parameters. This moves in the direction of defining cell types, as achieved for other brain regions such as the hippocampus.[35,36] We observed individual HD cells responding differently to light pulses, sound stimuli, and movement, mainly within their receptive fields (i.e., when each HD cell was most active); some HD cells were multimodal, whereas others were unresponsive. We identified both CR+ and CR− HD cells distributed within a CR mediolateral gradient. On average, CR+ cells had lower peak firing rates and narrower tuning widths compared with CR− cells, differences that were related to different intrinsic properties. We also identified an unusual kind of CR+ HD cell, the tortuosa cell, located within the C1ql2-lacking dorsomedial subregion of the ADn, which had descending axons and did not form collaterals in the TRN. Based on the tracing data, we suggest these cells target deep layers of the caudal MEC.

Receptive fields of HD cells promote arousal and attention

We observed HD cells responding robustly to light pulses, which resembled the "parallel channels" of retinal ganglion cells (RGCs).[37] Response latencies were similar to the light responses of neurons in the mouse dorsal lateral geniculate nucleus.[38] Given these similar response latencies and that the ADn receives direct input from the retina,[39,40] we suggest that, in addition to the main driving vestibular/proprioceptive inputs via the lateral mammillary nucleus, ADn HD cells may receive monosynaptic inputs from different types of RGCs and/or inputs from other retinorecipient areas such as within the pretectal complex.[41] Indeed, some pretectal nuclei project to the LD and could potentially form collaterals in the adjacent ADn.[42,43] The ON and OFF "inhibition" responses, which had longer latencies than ON and OFF "excitation," may arise from visually modulated pretectal GABAergic inputs. The bright light pulses we presented likely induced the pupillary light reflex (PLR). Indeed, pupil diameter has been shown to positively correlate with firing rates of thalamocortical neurons in both the ADn and lateral geniculate nucleus.[21,44] Intrinsically photosensitive (Opn-expressing) RGCs are the main drivers of the PLR and project to the pretectal

Figure 5. Connectivity of ADn subregions

(A) Schematic of a Cre-dependent retrograde AAV (rAAV-hSyn-DIO-EGFP) injection into the dorsocaudal region of the retrosplenial cortex (RSp) and presubiculum (PrS) of a C1ql2-Cre mouse.

(B) Confocal image of the ADn (case SH85) showing retrogradely labeled cells (GFP+, green) with minimal colocalization with CR (red). Note axons originating from the ADn heading laterally toward the TRN (e.g., arrows).

(C) Top, proportion of CR+ cells within the total population of retrogradely labeled GFP+ cells. Bottom, intensity profiles for GFP and CR.

(D) Left, injection site of a retrograde AAV (rAAV-hSyn-EGFP) in the deep layers of the MEC in a wild-type mouse. Middle and right, details of the injection site. Wolframin (WFS1, gray) and calbindin (CB, purple) were used to delineate MEC layer 2. PaS, parasubiculum.

(E) Widefield epifluorescence of a coronal brain section (case SH63; injection site as in D) containing retrogradely labeled GFP-expressing cells in the ADn (dashed area). Note descending axons originating from the medial ADn (e.g., arrows).

(F) Left, retrogradely labeled cells (GFP+, green) in the ADn (injection site as in D) had a similar distribution to CR (red). Case SH63, confocal maximum-intensity z-projection (9 μm thick). Top right, proportion of CR+ cells within the total population of GFP+ cells. Bottom right, intensity profiles for GFP and CR.

(G) Top, confocal image of the ADn (case SH97) showing C1ql2 (green), CR (magenta), and DAPI (blue). Bottom, enlarged view of the boxed region showing CR+ cells lacking detectable C1ql2 immunoreactivity (arrows).

(H) Proportions of C1ql2+/− and CR+/− ADn cells (n = 3 mice) from (G).

(I) Top, schematic of Cre-ON/Cre-OFF AAV injections into the ADn of C1ql2-Cre mice (Cre-ON: GFP; Cre-OFF: tdTomato). Middle, confocal image of a horizontal brain section (case SH114) containing Cre-positive GFP-labeled cells (green) in the ADn and Cre-negative tdTomato-labeled cells (red). Bottom, confocal image of a coronal brain section (case SH100) containing Cre-positive GFP-labeled cells (green) in the ADn and Cre-negative tdTomato-labeled cells (red). The dorsomedial ADn contained C1ql2-negative cells.

(J) Quantification of C1ql2-positive (GFP) and C1ql2-negative (tdTomato) cells (n = 2 mice) from (I).

Scale bars: (B), (D) left and middle, (E), and (F) 100 μm; (D) right, (H) top, and (G) 50 μm, and (H) bottom, 20 μm.

Please cite this article in press as: Hijazi et al., Diversity and sensorimotor specialization of head direction cells in the mouse thalamus, Current Biology (2026), https://doi.org/10.1016/j.cub.2026.05.026

CellPress
OPEN ACCESS

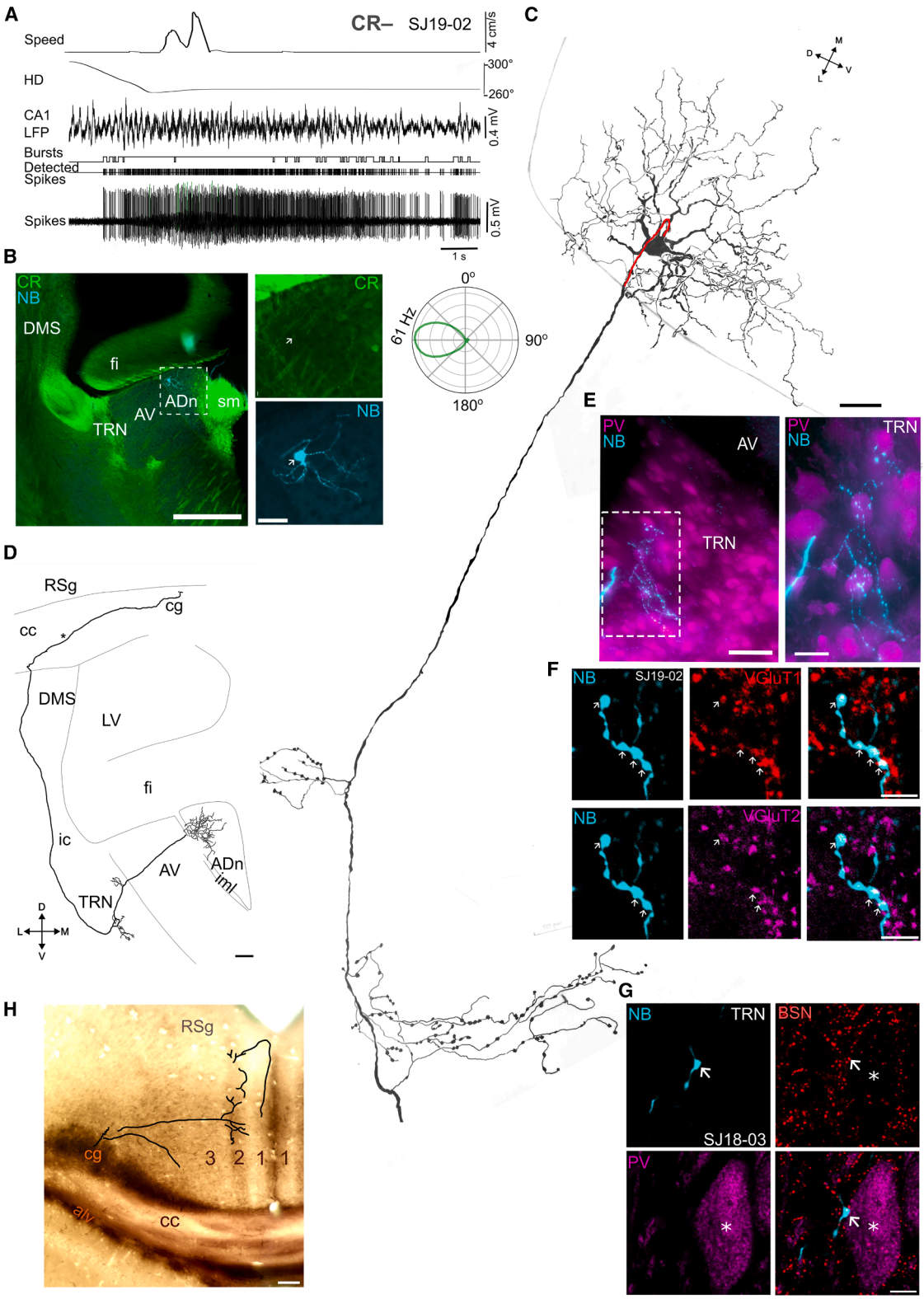

Figure 6. Axonal projections and synaptic target regions of ADn HD cells

(A) Firing patterns of a labeled HD cell (SJ19-02). Note the increase in firing during movement, coincident with theta oscillations present in the CA1 LFP. Bottom right, polar plot of the HD tuning curve with its peak firing rate indicated.

(legend continued on next page)

Please cite this article in press as: Hijazi et al., Diversity and sensorimotor specialization of head direction cells in the mouse thalamus, Current Biology (2026), https://doi.org/10.1016/j.cub.2026.05.026

complex.[45,46] Furthermore, Opn5-expressing RGCs have been shown to project to a specific zone close to the medial habenula,[47] which we suggest includes the CR-enriched medial ADn. These inputs may contribute to both the direct light responses and to their modulation by pupil size,[21] which is also a measure of arousal.[44,48] Lastly, the light responses of ADn cells may contribute to the positively and negatively visually modulated HD cells reported in the postsubiculum, a major postsynaptic target of the ADn.[30]

The sound-sensitive HD cells, which partially overlapped with the light-responsive cells, mainly increased their firing in response to sudden clicks; responses typically lasted longer than the duration of the clicks. ADn cells have previously been shown to respond to click stimuli in mice under isoflurane anesthesia,[21] suggesting that responses can be directly related to the sounds themselves; response profiles are likely dependent on the depth of anesthesia.[49] We observed that sound responses required the cell to be within its PFD, i.e., when the cell was already above its firing threshold (within its receptive field). We presented click stimuli from a fixed location in the room (allocentric cue), yet the mouse could be facing any direction, depending on where we detected the PFD. This is in contrast to light pulses, which were delivered directly in front of the mouse, regardless of the angle (egocentric cue). Some cells were additionally modulated during brief muscle twitches caused by the click stimulus (cross-modal summation), reminiscent of the startle response that activates the vestibular system.[31] We suggest that the main vestibular drivers of the HD signal promote these transient sensorimotor messages within the receptive field of each HD cell, updating the cortical mnemonic system with information about the current status of the body and environment, supporting cue-based realignment when navigating dynamic environments, which is important for path integration.

Taube[8] reported a weak positive correlation between the rat's linear speed and ADn HD cell firing rates. We detected HD cells that increased, decreased, or did not change their firing rate during movement on the running disc, suggesting that some HD cells may be modulated by running speed. The speed sensitivity is probably inherited from the presynaptic lateral mammillary nucleus, dorsal tegmental nucleus, and interpeduncular nucleus.[9,50–52] Speed cells have also been described in cortical regions postsynaptic to the ADn, including the EC,[53,54] which may depend on speed-modulated ADn HD cells.

CR distinguishes HD cell subpopulations

By combining juxtacellular labeling with immunohistochemistry, we found that HD cells in the medial ADn were typically CR+, whereas more lateral cells were predominantly CR−. The CR+ ADn cells form part of a stream of CR+ neurons extending along the midline of the mouse and human thalamus.[33,55,56] In general, CR+ HD cells had narrower directional tuning, lower firing rates, and produced fewer spikes per rebound burst. This is consistent with other midline thalamic CR+ neurons recorded in anesthetized mice.[57] In the midline paraventricular thalamic nucleus, CR+ neurons respond to transient changes in muscle tone, linked to changes in arousal.[33]

We found that CR+ cells preferentially targeted deep layers of the caudal MEC, whereas CR− cells innervated more anterior and dorsal cortical regions, including the dorsal part of the retrosplenial cortex and the presubiculum. This connectivity pattern complements Hintiryan et al.[14] who showed ADn subdivisions defined by their projection target, supporting the idea of multimodal HD streams conveying complementary sensorimotor messages. In the human thalamus, CR+ ADn cells are preferentially vulnerable to tau pathology,[56] a major hallmark of Alzheimer's disease. This raises the possibility that the gradual loss of CR+ HD cells during disease progression preferentially affects neural circuits of CR+ cells and their associated functions.

The subpopulation of HD cells with collaterals in the DMS was CR−. The ADn cells with collaterals in the DMS are likely responsible for striatal HD signals, as lesions of the anterior thalamus eliminate DMS HD signals.[58] We detected presynaptic ADn cell terminals in close apposition to cholinergic interneurons, suggesting that ADn HD cells may also indirectly modulate medium spiny neurons. ADn HD cells may also contribute to egocentric boundary responses observed in the DMS[59] to help guide movement away from barriers.

The CR+ tortuosa cells found in the C1ql2− dorsomedial ADn have the highest probability of being designated as a "cell type" because they represent a distinct subpopulation defined by a combination of parameters (distinct axonal projection pattern,

(B) Left, widefield epifluorescence micrograph of a 70-μm-thick coronal brain section showing part of the soma and dendrites of cell SJ19-02 (asterisk, NB, neurobiotin, cyan) in the lateral ADn. Right, enlarged view of the boxed region showing the soma (cyan, asterisk), which lacks detectable CR immunoreactivity (green).
(C) Full reconstruction of the soma and dendrites of cell SJ19-02 and axon collaterals in the TRN (only large terminals are shown). The axon originates from the medial side of the soma (highlighted in red). Reconstructed from 5 consecutive 70-μm-thick brain sections.
(D) A two-dimensional representation of the axon projection of SJ19-02 between the ADn and cingulum bundle (cg) (covering ~−0.10 to −0.58 mm AP). Asterisk, turning point of the axon. The horizontal bar indicates the end of the reconstructed portion.
(E) Left, maximum-intensity z-projection (37.8 μm thick, widefield epifluorescence) of an axon collateral in the TRN from cell SJ19-02 (neurobiotin, NB, cyan) within the parvalbumin (PV)-enriched TRN (magenta). Note the lack of PV cells in the adjacent AV. Right, enlarged view of the box region, maximum-intensity z-projection (46.5 μm thick).
(F) Boutons of the CR− HD cell SJ18-03 in the TRN (neurobiotin, NB, cyan, arrows) were immunopositive for both VGLUT1+ (red) and VGLUT2+ (magenta). Confocal maximum-intensity z-projection, 1.8 μm thick.
(G) A PV+ neuron (magenta) in the TRN is innervated by boutons (cyan) of a CR− HD cell (SJ18-03). Bassoon (red) indicates the expected location of synapses; single optical confocal image.
(H) A two-dimensional representation of the axon collaterals of SJ19-02 in the RSg originating from the main axon in the cg (partial reconstruction from 4 consecutive 70-μm-thick brain sections overlaid on one representative section). Note the highly branched pattern in layer 3, with axons reaching layer 2 as well as horizontally along layer 1 (axon terminals not shown).
Abbreviations: alv, alveus; cc, corpus callosum; LV, lateral ventricle; fi, fimbria; ic, internal capsule; iml, internal medullary lamina. Scale bars: (B) left, 500 μm; (D) and (H), 100 μm; (B) right, (C), and (E) left, 50 μm; and (E) right, (F), and (G), 5 μm.

Please cite this article in press as: Hijazi et al., Diversity and sensorimotor specialization of head direction cells in the mouse thalamus, Current Biology (2026), https://doi.org/10.1016/j.cub.2026.05.026

CellPress
OPEN ACCESS

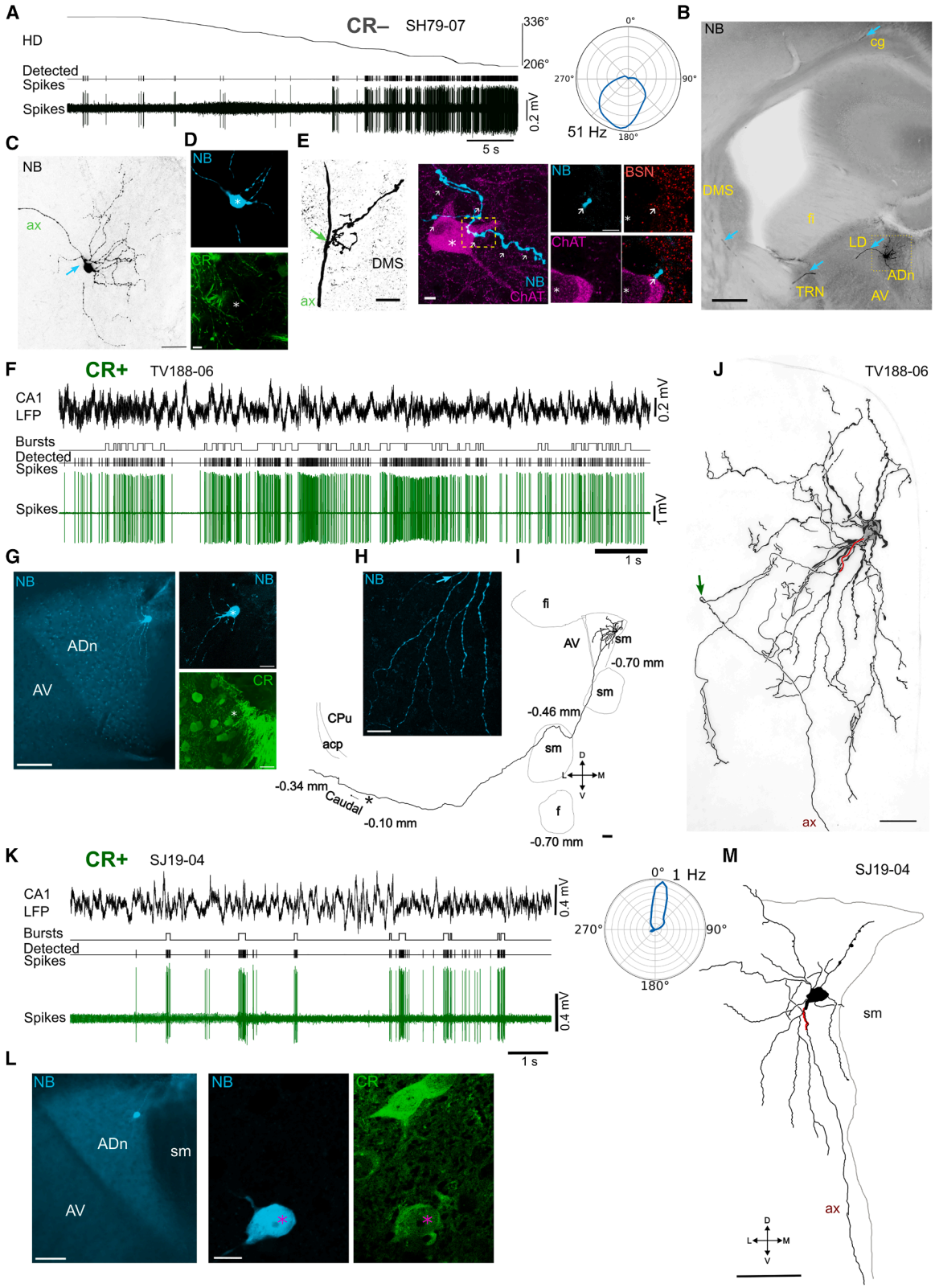

(legend on next page)

Please cite this article in press as: Hijazi et al., Diversity and sensorimotor specialization of head direction cells in the mouse thalamus, Current Biology (2026), https://doi.org/10.1016/j.cub.2026.05.026

narrow HD tuning, low peak firing rate, neurochemical profile, and dorsomedial position). Additional recorded cells are required to define the synaptic target regions of single-labeled tortuosa cells. Nevertheless, the tortuosa cells support the hypothesis that the ADn contains cell types, with each type receiving different inputs and conveying distinct responses to different sensorimotor inputs.

Conclusions

Our results reveal a rich microarchitecture within the ADn—a central hub of the HD network—providing novel insights into ADn cell diversity. Individual HD cells showed specializations in terms of their sensorimotor responses, connectivity, and neurochemical identity, with CR+ cells forming a mediolateral gradient. Our findings suggest that, in addition to their established vestibular/proprioceptive drivers, HD cells encode the salience or behavioral relevance of transient sensorimotor events, as reflected by the differential responses to light pulses, sound, and movement within their receptive fields. This is consistent with recent evidence that HD cell activity is modulated by sensory signals and behavioral states.[21] Therefore, the firing patterns within these receptive fields, including the burst duration and frequency, are likely modulated by arousal, potentially updating the cortical mnemonic system with salient sensorimotor information arising from the body and environment to support spatial navigation. We suggest that this activity may contribute to the awareness of spatial orientation. Moreover, several autism- and schizophrenia-associated genes are enriched in the ADn, and selective knockdown of such risk genes in the mouse ADn promotes hyperexcitability.[34] We therefore hypothesize that altered ADn activity—particularly the integration of visual and auditory sensorimotor signals—may contribute to particular behavioral features associated with these conditions, including altered attention, atypical gaze, and sensory hyperreactivity.[60,61] Altered burst firing or sustained activity following sensorimotor stimuli conveyed via ADn HD cells could consequently influence the stability or salience of directional representations, potentially affecting the awareness of orientation, as is the case for dizziness.[20,62,63] Taken together, we propose that different kinds of ADn HD cells encode various aspects of attention and arousal, based on the repeated responses to salient sensorimotor events and that the dynamic patterns of spikes (including burst firing) within HD cell receptive fields represent distinct signals from the environment and body.

RESOURCE AVAILABILITY

Lead contact

Requests for further information and resources should be directed to and will be fulfilled by the lead contact, Tim Viney (tim.viney@pharm.ox.ac.uk).

Materials availability

This study did not generate new unique reagents.

Data and code availability

- Electrophysiological data have been deposited in https://doi.org/10.5281/zenodo.20124105.[64]
- Code can be found at https://github.com/hasselmonians/Jiang_Hijazi_2025 and https://github.com/neuralcircuitsTV/spikes_juxta.
- Any additional information required to reanalyze the data reported in this paper is available from the lead contact upon request.

ACKNOWLEDGMENTS

We thank Barbara Sárkány, Francesca Corsi, Aditi Athreya, and Kathryn Holland for help with tissue processing; Brook Perry for advice on implementing the inertial measurement unit; and Martyn Preston for building the light and sound modules. We also thank Patvitra Reanchareonsuk for help with 2D reconstructions. Funding was provided by the Alzheimer's Society grant 522 AS-PhD-19a-010 (T.J.V.), Medical Research Council grants MR/R011567/1 and MR/Z504518/1 (T.J.V.), The John Fell Fund grant 0013781 (T.J.V.), UKRI

Figure 7. Specialized axonal projection patterns of CR+ and CR– HD cells

(A) Left, firing patterns of juxtacellularly labeled HD cell SH79-09 over a range of HDs. Right, polar plot of the HD tuning curve with its peak firing rate indicated.
(B) Widefield epifluorescence micrograph (reverse contrast) of a coronal brain section showing the soma and partial dendritic tree of neurobiotin-labeled cell SH79-07 in the lateral ADn, along with the axon (e.g., cyan arrows) projecting to the TRN, DMS, and RSg via the cingulum.
(C) Enlarged view of the soma and partial dendrites of cell SH79-07 showing the origin of the axon (arrow). Confocal maximum-intensity z-projection (51.2 μm thick).
(D) The soma of cell SH79-07 (cyan, asterisk) lacked CR immunoreactivity (green). Confocal maximum-intensity z-projection (6 μm thick).
(E) Left, axon collateral (arrow) arising from the main axon (ax) of cell SH79-07 in the DMS. Confocal maximum-intensity z-projection (10 μm thick). Middle, axon terminals (neurobiotin, cyan, e.g., arrows) in close apposition to a ChAT+ neuron (asterisk, magenta) in the DMS. Right, single optical section showing innervation of the ChAT+ neuron by a bouton (NB, arrow), indicated by bassoon-immunoreactive (BSN+) puncta (red).
(F) Firing patterns of the juxtacellularly labeled ADn cell (TV188-06) in its PFD.
(G) Left, widefield epifluorescence micrograph of a coronal brain section showing the soma and partial dendritic tree of cell TV188-06 (asterisk, NB, neurobiotin, cyan) in the dorsomedial ADn. Right, the cell was immunopositive for CR (green, asterisk).
(H) Detail of dendrites (confocal maximum-intensity z-projection, 54.5 μm thick). Arrow, axon.
(I) A two-dimensional representation of the descending axon of TV188-06 between the ADn and the endopiriform cortex (covering ∼−0.10 to −0.70 mm AP). Asterisk, turning point of the axon.
(J) 2D reconstruction of the soma and dendrites of TV188-06 (from 4 consecutive 70-μm-thick sections). The axon originated from the soma (highlighted in red). Arrow, looping point of the axon where it changes direction. The soma is semi-opaque in order to visualize the dendrites. Note that some dendritic segments were left unconnected due to weak labeling in some sections.
(K) Left, firing patterns of a labeled ADn HD cell (SJ19-04) in its PFD. Right, polar plot of the HD tuning curve with peak firing rate indicated.
(L) Left, widefield epifluorescence micrograph of a coronal brain section showing the soma and partial dendritic tree of cell SJ19-04 (asterisk, NB, neurobiotin, cyan) in the dorsomedial ADn. Right, the soma (cyan) was immunopositive for CR (green, asterisk; single optical section).
(M) Partial 2D reconstruction of the soma and dendrites from one 70-μm-thick section. The axon originated from a dendrite (highlighted in red) and headed ventrally.
Abbreviations: acp, anterior commissure, posterior; ax, axon; cg, cingulum; CPU, caudate putamen (striatum); f, fornix; fi, fimbria; sm, stria medullaris; NB, neurobiotin. Scale bars: (B), 300 μm; (C), (J), and (M) 50 μm; (D) and (L) right, 10 μm; (E), 5 μm; (G) left, (I), and (L) left, 100 μm; (H) and (G) right, 20 μm.

grant EP/Z001358/1 (T.J.V. and S.H.), Alzheimer's Research UK ARUK-RF2023B-026 (S.H.), ARUK Thames VValley Small Equipment award AVR01965 (S.H.), NIH R01 MH120073 (M.E.H.), US Office of Naval Research MURI N00014-1-19-2571 (M.E.H.), and NIH F32MH139270 (P.A.L.). S.H. was supported by a Blaschko Fellowship from the Department of Pharmacology, Oxford. S.J. was supported by a Clarendon Scholarship.

AUTHOR CONTRIBUTIONS

Conceptualization, S.H., S.J., and T.J.V.; methodology, S.H., S.J., and T.J.V.; software, S.H., S.J., P.A.L., and T.J.V.; validation, S.H., S.J., P.A.L., M.E.H., and T.J.V.; formal analysis, S.H., S.J., M.S.W., J.Q., and T.J.V.; investigation, S.H., S.J., M.S.W., J.Q., P.A.L., M.E.H., and T.J.V.; resources. S.H., M.E.H., and T.J.V.; data curation, S.H., S.J., and T.J.V.; writing—original draft, S.H., S.J., and T.J.V.; writing—review and editing, S.H., S.J., M.S.W., J.Q., P.A.L., M.E.H., and T.J.V.; visualization, S.H., S.J., M.S.W., J.Q., and T.J.V.; supervision, T.J.V.; project administration, T.J.V.; and funding acquisition, S.H. and T.J.V.

DECLARATION OF INTERESTS

The authors declare no competing interests.

STAR★METHODS

Detailed methods are provided in the online version of this paper and include the following:

- KEY RESOURCES TABLE
- EXPERIMENTAL MODEL AND SUBJECT DETAILS
- METHOD DETAILS
  - Surgical procedures
  - *In vivo* recordings and juxtacellular labeling
  - Sensory stimuli
  - Slice physiology
  - Histology
  - Microscopy
  - Quantification of ADn cells
  - Analysis of electrophysiological data
  - Statistics

SUPPLEMENTAL INFORMATION

Supplemental information can be found online at https://doi.org/10.1016/j.cub.2026.05.026.

Received: October 3, 2025
Revised: April 7, 2026
Accepted: May 12, 2026

REFERENCES

1. Taube, J.S. (2007). The head direction signal: origins and sensory-motor integration. Annu. Rev. Neurosci. *30*, 181–207. https://doi.org/10.1146/annurev.neuro.29.051605.112854.
2. Alexander, A.S., Robinson, J.C., Stern, C.E., and Hasselmo, M.E. (2023). Gated transformations from egocentric to allocentric reference frames involving retrosplenial cortex, entorhinal cortex, and hippocampus. Hippocampus *33*, 465–487. https://doi.org/10.1002/hipo.23513.
3. Clark, B.J., LaChance, P.A., Winter, S.S., Mehlman, M.L., Butler, W., LaCour, A., and Taube, J.S. (2024). Comparison of head direction cell firing characteristics across thalamo-parahippocampal circuitry. Hippocampus *34*, 168–196. https://doi.org/10.1002/hipo.23596.
4. O'Keefe, J., and Nadel, L. (1978). The Hippocampus as a Cognitive Map (Clarendon Press).
5. Buzsáki, G., and Moser, E.I. (2013). Memory, navigation and theta rhythm in the hippocampal-entorhinal system. Nat. Neurosci. *16*, 130–138. https://doi.org/10.1038/nn.3304.
6. Gibson, B., Butler, W.N., and Taube, J.S. (2013). The head-direction signal is critical for navigation requiring a cognitive map but not for learning a spatial habit. Curr. Biol. *23*, 1536–1540. https://doi.org/10.1016/j.cub.2013.06.030.
7. Clark, B.J., and Harvey, R.E. (2016). Do the anterior and lateral thalamic nuclei make distinct contributions to spatial representation and memory? Neurobiol. Learn. Mem. *133*, 69–78. https://doi.org/10.1016/j.nlm.2016.06.002.
8. Taube, J.S. (1995). Head direction cells recorded in the anterior thalamic nuclei of freely moving rats. J. Neurosci. *15*, 70–86. https://doi.org/10.1523/JNEUROSCI.15-01-00070.1995.
9. Stackman, R.W., and Taube, J.S. (1998). Firing properties of rat lateral mammillary single units: head direction, head pitch, and angular head velocity. J. Neurosci. *18*, 9020–9037. https://doi.org/10.1523/JNEUROSCI.18-21-09020.1998.
10. Shibata, H. (1993). Direct projections from the anterior thalamic nuclei to the retrohippocampal region in the rat. J. Comp. Neurol. *337*, 431–445. https://doi.org/10.1002/cne.903370307.
11. Shibata, H. (1993). Efferent projections from the anterior thalamic nuclei to the cingulate cortex in the rat. J. Comp. Neurol. *330*, 533–542. https://doi.org/10.1002/cne.903300409.
12. Taube, J.S., Muller, R.U., and Ranck, J.B., Jr. (1990). Head-direction cells recorded from the postsubiculum in freely moving rats. I. Description and quantitative analysis. J. Neurosci. *10*, 420–435. https://doi.org/10.1523/JNEUROSCI.10-02-00420.1990.
13. Tukker, J.J., Tang, Q., Burgalossi, A., and Brecht, M. (2015). Head-Directional Tuning and Theta Modulation of Anatomically Identified Neurons in the Presubiculum. J. Neurosci. *35*, 15391–15395. https://doi.org/10.1523/JNEUROSCI.0685-15.2015.
14. Hintiryan, H., Rudd, M., Nanda, S., Gutierrez, A.E., Lo, D., Boesen, T., Garcia, L., Sun, J., Estrada, C., Mun, H.S., et al. (2025). Distinct subnetworks of the mouse anterior thalamic nuclei. Nat. Commun. *16*, 6018. https://doi.org/10.1038/s41467-025-60774-6.
15. Van Groen, T., and Wyss, J.M. (1995). Projections from the anterodorsal and anteroventral nucleus of the thalamus to the limbic cortex in the rat. J. Comp. Neurol. *358*, 584–604. https://doi.org/10.1002/cne.903580411.
16. Shibata, H. (1998). Organization of projections of rat retrosplenial cortex to the anterior thalamic nuclei. Eur. J. Neurosci. *10*, 3210–3219. https://doi.org/10.1046/j.1460-9568.1998.00328.x.
17. van Groen, T., and Wyss, J.M. (1990). The postsubicular cortex in the rat: characterization of the fourth region of the subicular cortex and its connections. Brain Res. *529*, 165–177. https://doi.org/10.1016/0006-8993(90)90824-U.
18. Oulé, M., Badrinarayanan, S., Sundar-Maccagno, R., and Brandon, M.P. (2025). Medial entorhinal VIP-expressing interneurons receive input from the thalamic anterior dorsal nucleus and are critical for spatial memory. Proc. Natl. Acad. Sci. USA *122*, e2425024122. https://doi.org/10.1073/pnas.2425024122.
19. Zugaro, M.B., Arleo, A., Déjean, C., Burguière, E., Khamassi, M., and Wiener, S.I. (2004). Rat anterodorsal thalamic head direction neurons depend upon dynamic visual signals to select anchoring landmark cues. Eur. J. Neurosci. *20*, 530–536. https://doi.org/10.1111/j.1460-9568.2004.03512.x.
20. Grieves, R.M., Shinder, M.E., Rosow, L.K., Kenna, M.S., and Taube, J.S. (2022). The Neural Correlates of Spatial Disorientation in Head Direction Cells. eNeuro *9*. ENEURO.0174-22.2022. https://doi.org/10.1523/ENEURO.0174-22.2022.
21. Blanco-Hernández, E., Balsamo, G., Preston-Ferrer, P., and Burgalossi, A. (2024). Sensory and behavioral modulation of thalamic head-direction cells. Nat. Neurosci. *27*, 28–33. https://doi.org/10.1038/s41593-023-01506-1.

22. Shinder, M.E., and Taube, J.S. (2011). Active and passive movement are encoded equally by head direction cells in the anterodorsal thalamus. J. Neurophysiol. *106*, 788–800. https://doi.org/10.1152/jn.01098.2010.

23. Shinder, M.E., and Taube, J.S. (2014). Resolving the active versus passive conundrum for head direction cells. Neuroscience *270*, 123–138. https://doi.org/10.1016/j.neuroscience.2014.03.053.

24. Knierim, J.J., Kudrimoti, H.S., and McNaughton, B.L. (1995). Place cells, head direction cells, and the learning of landmark stability. J. Neurosci. *15*, 1648–1659. https://doi.org/10.1523/JNEUROSCI.15-03-01648.1995.

25. Asumbisa, K., Peyrache, A., and Trenholm, S. (2022). Flexible cue anchoring strategies enable stable head direction coding in both sighted and blind animals. Nat. Commun. *13*, 5483. https://doi.org/10.1038/s41467-022-33204-0.

26. Fallahnezhad, M., Le Mero, J., Zenelaj, X., Vincent, J., Rochefort, C., and Rondi-Reig, L. (2023). Cerebellar control of a unitary head direction sense. Proc. Natl. Acad. Sci. USA *120*, e2214539120. https://doi.org/10.1073/pnas.2214539120.

27. Jiang, S., Hijazi, S., Sárkány, B., Gautsch, V.G., LaChance, P.A., Hasselmo, M.E., Bannerman, D., and Viney, T.J. (2025). Pathological tau alters head direction signaling and induces spatial disorientation. Cell Rep. *44*, 116610. https://doi.org/10.1016/j.celrep.2025.116610.

28. Yoder, R.M., and Taube, J.S. (2009). Head direction cell activity in mice: robust directional signal depends on intact otolith organs. J. Neurosci. *29*, 1061–1076. https://doi.org/10.1523/JNEUROSCI.1679-08.2009.

29. Zugaro, M.B., Arleo, A., Berthoz, A., and Wiener, S.I. (2003). Rapid spatial reorientation and head direction cells. J. Neurosci. *23*, 3478–3482. https://doi.org/10.1523/JNEUROSCI.23-08-03478.2003.

30. Siegenthaler, D., Denny, H., Carrasco, S.S., Mayer, J.L., Levenstein, D., Peyrache, A., Trenholm, S., and Macé, É. (2025). Visual objects refine head direction coding. Science *389*, eadu9828. https://doi.org/10.1126/science.adu9828.

31. Yeomans, J.S., Li, L., Scott, B.W., and Frankland, P.W. (2002). Tactile, acoustic and vestibular systems sum to elicit the startle reflex. Neurosci. Biobehav. Rev. *26*, 1–11. https://doi.org/10.1016/S0149-7634(01)00057-4.

32. Kapustina, M., Zhang, A.A., Tsai, J.Y.J., Bristow, B.N., Kraus, L., Sullivan, K.E., Erwin, S.R., Wang, L., Stach, T.R., Clements, J., et al. (2024). The cell-type-specific spatial organization of the anterior thalamic nuclei of the mouse brain. Cell Rep. *43*, 113842. https://doi.org/10.1016/j.celrep.2024.113842.

33. Mátyás, F., Komlósi, G., Babiczky, Á., Kocsis, K., Barthó, P., Barsy, B., Dávid, C., Kanti, V., Porrero, C., Magyar, A., et al. (2018). A highly collateralized thalamic cell type with arousal-predicting activity serves as a key hub for graded state transitions in the forebrain. Nat. Neurosci. *21*, 1551–1562. https://doi.org/10.1038/s41593-018-0251-9.

34. Roy, D.S., Zhang, Y., Aida, T., Choi, S., Chen, Q., Hou, Y., Lea, N.E., Skaggs, K.M., Quay, J.C., Liew, M., et al. (2021). Anterior thalamic dysfunction underlies cognitive deficits in a subset of neuropsychiatric disease models. Neuron *109*, 2590–2603.e13. https://doi.org/10.1016/j.neuron.2021.06.005.

35. Viney, T.J., Lasztoczi, B., Katona, L., Crump, M.G., Tukker, J.J., Klausberger, T., and Somogyi, P. (2013). Network state-dependent inhibition of identified hippocampal CA3 axo-axonic cells in vivo. Nat. Neurosci. *16*, 1802–1811. https://doi.org/10.1038/nn.3550.

36. Lapray, D., Lasztoczi, B., Lagler, M., Viney, T.J., Katona, L., Valenti, O., Hartwich, K., Borhegyi, Z., Somogyi, P., and Klausberger, T. (2012). Behavior-dependent specialization of identified hippocampal interneurons. Nat. Neurosci. *15*, 1265–1271. https://doi.org/10.1038/nn.3176.

37. Roska, B., and Werblin, F. (2001). Vertical interactions across ten parallel, stacked representations in the mammalian retina. Nature *410*, 583–587. https://doi.org/10.1038/35069068.

38. Piscopo, D.M., El-Danaf, R.N., Huberman, A.D., and Niell, C.M. (2013). Diverse visual features encoded in mouse lateral geniculate nucleus. J. Neurosci. *33*, 4642–4656. https://doi.org/10.1523/jneurosci.5187-12.2013.

39. Morin, L.P., and Studholme, K.M. (2014). Retinofugal projections in the mouse. J. Comp. Neurol. *522*, 3733–3753. https://doi.org/10.1002/cne.23635.

40. Conrad, C.D., and Stumpf, W.E. (1975). Direct visual input to the limbic system: Crossed retinal projections to the nucleus anterodorsalis thalami in the tree shrew. Exp. Brain Res. *23*, 141–149. https://doi.org/10.1007/BF00235456.

41. Allen, A.E., Brown, T.M., and Lucas, R.J. (2011). A distinct contribution of short-wavelength-sensitive cones to light-evoked activity in the mouse pretectal olivary nucleus. J. Neurosci. *31*, 16833–16843. https://doi.org/10.1523/jneurosci.2505-11.2011.

42. Thompson, S.M., and Robertson, R.T. (1987). Organization of subcortical pathways for sensory projections to the limbic cortex. II. Afferent projections to the thalamic lateral dorsal nucleus in the rat. J. Comp. Neurol. *265*, 189–202. https://doi.org/10.1002/cne.902650204.

43. Bokor, H., Frère, S.G.A., Eyre, M.D., Slézia, A., Ulbert, I., Lüthi, A., and Acsády, L. (2005). Selective GABAergic Control of Higher-Order Thalamic Relays. Neuron *45*, 929–940. https://doi.org/10.1016/j.neuron.2005.01.048.

44. Molnár, B., Sere, P., Bordé, S., Koós, K., Zsigri, N., Horváth, P., and Lőrincz, M.L. (2021). Cell Type-Specific Arousal-Dependent Modulation of Thalamic Activity in the Lateral Geniculate Nucleus. Cereb. Cortex Commun. *2*, tgab020. https://doi.org/10.1093/texcom/tgab020.

45. Viney, T.J., Balint, K., Hillier, D., Siegert, S., Boldogkoi, Z., Enquist, L.W., Meister, M., Cepko, C.L., and Roska, B. (2007). Local retinal circuits of melanopsin-containing ganglion cells identified by transsynaptic viral tracing. Curr. Biol. *17*, 981–988. https://doi.org/10.1016/j.cub.2007.04.058.

46. Chen, S.K., Badea, T.C., and Hattar, S. (2011). Photoentrainment and pupillary light reflex are mediated by distinct populations of ipRGCs. Nature *476*, 92–95. https://doi.org/10.1038/nature10206.

47. Fernandez, D.C., Fogerson, P.M., Lazzerini Ospri, L., Thomsen, M.B., Layne, R.M., Severin, D., Zhan, J., Singer, J.H., Kirkwood, A., Zhao, H., et al. (2018). Light Affects Mood and Learning through Distinct Retina-Brain Pathways. Cell *175*, 71–84.e18. https://doi.org/10.1016/j.cell.2018.08.004.

48. Petty, G.H., and Bruno, R.M. (2024). Attentional modulation of secondary somatosensory and visual thalamus of mice. eLife *13*, RP97188. https://doi.org/10.7554/eLife.97188.

49. Detsch, O., Vahle-Hinz, C., Kochs, E., Siemers, M., and Bromm, B. (1999). Isoflurane induces dose-dependent changes of thalamic somatosensory information transfer. Brain Res. *829*, 77–89. https://doi.org/10.1016/s0006-8993(99)01341-4.

50. Sharp, P.E., Turner-Williams, S., and Tuttle, S. (2006). Movement-related correlates of single cell activity in the interpeduncular nucleus and habenula of the rat during a pellet-chasing task. Behav. Brain Res. *166*, 55–70. https://doi.org/10.1016/j.bbr.2005.07.004.

51. Taube, J.S., and Bassett, J.P. (2003). Persistent neural activity in head direction cells. Cereb. Cortex *13*, 1162–1172. https://doi.org/10.1093/cercor/bhg102.

52. Taube, J.S., Butler, W.N., Dumont, J.R., Graham, J.A., Marcroft, J.L., Shinder, M.E., Stackman, R.W., and Yoder, R.M. (2025). The head-direction signal is generated from two types of head direction cells in brainstem nuclei. Nat. Commun. *16*, 9755. https://doi.org/10.1038/s41467-025-63968-0.

53. Kropff, E., Carmichael, J.E., Moser, M.B., and Moser, E.I. (2015). Speed cells in the medial entorhinal cortex. Nature *523*, 419–424. https://doi.org/10.1038/nature14622.

54. Hinman, J.R., Brandon, M.P., Climer, J.R., Chapman, G.W., and Hasselmo, M.E. (2016). Multiple Running Speed Signals in Medial Entorhinal Cortex. Neuron *91*, 666–679. https://doi.org/10.1016/j.neuron.2016.06.027.

55. Viena, T.D., Rasch, G.E., Silva, D., and Allen, T.A. (2021). Calretinin and calbindin architecture of the midline thalamus associated with

prefrontal-hippocampal circuitry. Hippocampus *31*, 770–789. https://doi.org/10.1002/hipo.23271.

56. Sárkány, B., Dávid, C., Hortobágyi, T., Gombás, P., Somogyi, P., Acsády, L., and Viney, T.J. (2024). Early and selective localization of tau filaments to glutamatergic subcellular domains within the human anterodorsal thalamus. Acta Neuropathol. *147*, 98. https://doi.org/10.1007/s00401-024-02749-3.
57. Lara-Vásquez, A., Espinosa, N., Durán, E., Stockle, M., and Fuentealba, P. (2016). Midline thalamic neurons are differentially engaged during hippocampus network oscillations. Sci. Rep. *6*, 29807. https://doi.org/10.1038/srep29807.
58. Mehlman, M.L., Winter, S.S., Valerio, S., and Taube, J.S. (2019). Functional and anatomical relationships between the medial precentral cortex, dorsal striatum, and head direction cell circuitry. I. Recording studies. J. Neurophysiol. *121*, 350–370. https://doi.org/10.1152/jn.00143.2018.
59. Hinman, J.R., Chapman, G.W., and Hasselmo, M.E. (2019). Neuronal representation of environmental boundaries in egocentric coordinates. Nat. Commun. *10*, 2772. https://doi.org/10.1038/s41467-019-10722-y.
60. Robertson, C.E., and Baron-Cohen, S. (2017). Sensory perception in autism. Nat. Rev. Neurosci. *18*, 671–684. https://doi.org/10.1038/nrn.2017.112.
61. Brenner, C.A., Krishnan, G.P., Vohs, J.L., Ahn, W.-Y., Hetrick, W.P., Morzorati, S.L., and O'Donnell, B.F. (2009). Steady State Responses: Electrophysiological Assessment of Sensory Function in Schizophrenia. Schizophr. Bull. *35*, 1065–1077. https://doi.org/10.1093/schbul/sbp091.
62. Cronin, T., Arshad, Q., and Seemungal, B.M. (2017). Vestibular Deficits in Neurodegenerative Disorders: Balance, Dizziness, and Spatial Disorientation. Front. Neurol. *8*, 538. https://doi.org/10.3389/fneur.2017.00538.
63. Valerio, S., and Taube, J.S. (2016). Head Direction Cell Activity Is Absent in Mice without the Horizontal Semicircular Canals. J. Neurosci. *36*, 741–754. https://doi.org/10.1523/JNEUROSCI.3790-14.2016.
64. Hijazi, S., Jiang, S., and Viney, T.J. (2026). Extracellular recordings and juxtacellular labelling with glass electrodes in the mouse anterodorsal thalamic nucleus and hippocampus. Zenodo. https://doi.org/10.5281/zenodo.20124105.
65. Viney, T.J., Sarkany, B., Ozdemir, A.T., Hartwich, K., Schweimer, J., Bannerman, D., and Somogyi, P. (2022). Spread of pathological human Tau from neurons to oligodendrocytes and loss of high-firing pyramidal neurons in aging mice. Cell Rep. *41*, 111646. https://doi.org/10.1016/j.celrep.2022.111646.
66. Viney, T.J., Salib, M., Joshi, A., Unal, G., Berry, N., and Somogyi, P. (2018). Shared rhythmic subcortical GABAergic input to the entorhinal cortex and presubiculum. eLife *7*, e34395. https://doi.org/10.7554/eLife.34395.
67. Clark, B.J., Harris, M.J., and Taube, J.S. (2012). Control of anterodorsal thalamic head direction cells by environmental boundaries: comparison with conflicting distal landmarks. Hippocampus *22*, 172–187. https://doi.org/10.1002/hipo.20880.
68. Blair, H.T., Lipscomb, B.W., and Sharp, P.E. (1997). Anticipatory time intervals of head-direction cells in the anterior thalamus of the rat: implications for path integration in the head-direction circuit. J. Neurophysiol. *78*, 145–159. https://doi.org/10.1152/jn.1997.78.1.145.
69. Li, Z., Huang, J.J., Zhang, Y.E., Su, K.K., Peng, B., Seo, B.M., Zhang, L.I., and Tao, H.W. (2025). Direction-selective laterodorsal thalamic nucleus encodes optic flow and turning in spatial navigation. Neuron *113*, 3424–3440.e8. https://doi.org/10.1016/j.neuron.2025.07.014.

Please cite this article in press as: Hijazi et al., Diversity and sensorimotor specialization of head direction cells in the mouse thalamus, Current Biology (2026), https://doi.org/10.1016/j.cub.2026.05.026

STAR★METHODS

KEY RESOURCES TABLE

REAGENT or RESOURCE	SOURCE	IDENTIFIER
Antibodies		
Rabbit anti-calretinin	Swant	7699/3H; RRID: AB_10000321
Rabbit anti-calretinin	ABclonal	A21965
Rabbit anti-PCP4	Santa Cruz Biotech	sc-74816; RRID: AB_2236566
Guinea pig anti-vGLUT1	Synaptic Systems GmbH	135 304; RRID: AB_887878
Guinea pig anti-vGLUT2	Synaptic Systems GmbH	135 404; RRID: AB_887884
Mouse anti-bassoon	StressGen	VAM-PS003; RRID: AB_10618753
Rabbit anti-ChAT	Synaptic Systems	297 013; RRID: AB_2620040
Goat anti-ChAT	Chemicon	AB144P; RRID: AB_2079751
Guinea pig anti-parvalbumin	Synaptic Systems	195 004; RRID: AB_2156476
Rabbit anti-C1ql2	Novus Biologicals	NBP2-34090; RRID: AB_3285559
Mouse anti-NeuN	EMD Millipore Corp.	MAB377, lot 3713321; RRID: AB_2298772
Rabbit anti-WFS1	Proteintech	11558-1-AP; RRID: AB_2216046
Guinea pig anti-calbindin	Synaptic Systems	214-004, lot 1-14; RRID: AB_10550535
Chemicals, peptides, and recombinant proteins		
retroAAV-hSyn-EGFP	Addgene	50465
RetroAAV-EF1a-DIO-EYFP	Addgene	27056
AAV-1-hSyn1-dlox-EGFP(rev)-dlox-WPRE-hGHp(A)	Virus Vector Facility	VVF115
AAV-8-hEF1α-dlox-dTomato-EGFP(rev)-dlox-WPRE-hGHp(A)	Virus Vector Facility	VVF198
AAV-1-hSyn1-chI-loxP-mRuby3-loxP-SV40p(A)	Virus Vector Facility	VVF160
Neurobiotin tracer	Vector Laboratories	SP-1120; RRID: AB_2313575
Isoflurane inhalation anesthesia	Teva Ltd.	products.tevauk.com/p/Category?id=185
Vetergesic (buprenorphine)	Ceva	56454-04
Marcain (bupivacaine)	Aspen	PS22421
Metacam (meloxicam)	Boerhinger Ingelheim	N/A
Refobacin bone cement	Zimmer Biomet	3003940002-3
Tetric EvoFlow dental cement	Ivoclar Vivadent	A1
DiI tracer	Life Technologies	V22889
Normal horse serum	Vector Laboratories	S-2000
Normal goat serum	Vector Laboratories	S-1000
Critical commercial assays		
Vectastain ABC Elite kit	Vector Laboratories	PK6100; RRID: AB_2336819
Vectashield Antifade Mounting Medium	Vector Laboratories	H-1000; RRID: AB_2336789
Deposited data		
Electrophysiological data	Zenodo	https://doi.org/10.5281/zenodo.20124105
Code and data	Github	https://github.com/neuralcircuitsTV/spikes_juxta
Experimental models: Organisms/strains		
C57BL6j mice	Charles River Laboratories	www.criver.com/
C1QL2-IRES-Cre mice (C57BL/6-C1ql2$^{em1(cre)Gfng}$/J)	Jackson Laboratory	www.jax.org/strain/036955
Software and algorithms		
FIJI (ImageJ)	NIH	imagej.net/software/fiji/
MATLAB	Mathworks	www.mathworks.com/products/matlab.html
Python		www.python.org/
Zen Black, Zen Blue	Zeiss	www.zeiss.co.uk

(*Continued on next page*)

Please cite this article in press as: Hijazi et al., Diversity and sensorimotor specialization of head direction cells in the mouse thalamus, Current Biology (2026), https://doi.org/10.1016/j.cub.2026.05.026

Continued

REAGENT or RESOURCE	SOURCE	IDENTIFIER
Spike2	Cambridge Electronic Design	ced.co.uk/
GraphPad Prism 7	GraphPad Software	www.graphpad.com/
Wolfram Mathematica		www.wolfram.com/mathematica/
Igor Pro-9.0	Wavemetrics	www.wavemetrics.com/software/igor-pro-9
Open Ephys GUI	Open Ephys	https://open-ephys.org/gui
Other		
A1x16-poly 2s silicon probe	NeuroNexus	neuronexus.com/

EXPERIMENTAL MODEL AND SUBJECT DETAILS

All procedures involving experimental animals were under approved personal and project licenses according to UK Animals (Scientific Procedure) Act 1986 and associated regulations. Experiments were conducted with adult male and female C57Bl/6J mice and heterozygous C1QL2-IRES-Cre mice (C57BL/6-C1ql2$^{em1(cre)Gfng}$/J, strain #036955, The Jackson Laboratory). A total of 66 mice were used in this study. We performed *in vivo* recordings from 45 mice, including 19 that were injected with AAVs (reported in Jiang et al.[27]) (Tables S1 and S4). We performed *ex vivo* recordings in brain slices from 8 mice, and performed additional tracing experiments in 13 mice, some of which were used for immunohistochemical tests.

METHOD DETAILS

Surgical procedures

In vivo *extracellular recordings in head-fixed mice*

Surgical procedures were performed as previously described.[65,66] Briefly, mice were induced with 4% isoflurane (IsoFlo, Zoetis Inc.) in carboxygen (flow rate 2L/min) and maintained with 1-2% isoflurane following a subcutaneous injection of buprenorphine (at 0.1 mg/kg, Vetergesic). The scalp was clipped, sterilized, and injected with bupivacaine (Marcain). Following exposure of the skull, four craniotomy sites and three screws sites were marked and drilled based on stereotaxic coordinates. Craniotomy sites (in mm from Bregma): hippocampal CA1, -2.5 to -2.3 anteroposterior (AP) +1.5 mediolateral (ML), and -2.3 AP -1.5 ML; ADn, -0.85 AP ±0.75 ML. Two M1.2 x 3 screws (Precision Technology Supplies Ltd) with a soldered pin were fixed to the skull above the cerebellum for ground/reference and securing the head plate. One or two M1.2 x 2 screws were fixed above the motor cortex (+1.5 AP, ±1.7 ML) to support the head plate. Screws were sealed with Refobacin bone cement, and a machined glass-reinforced plastic D-shaped headplate (0.7 g, custom made at the Department of Physics, Oxford University) was positioned over the screws and secured with the cement. Craniotomies and duratomies were performed at each site. Craniotomy sites were protected with silicon. In 7 mice an electromyogram (EMG) was recorded through a twisted stainless-steel wire under the skin to reach the neck muscles, which was positioned by making a small incision in the skin at the dorsal neck region. Finally, mice were administered a subcutaneous dose of meloxicam (at 5 mg/kg, Metacam), and were monitored during recovery on a heat pad.

Anterograde and retrograde tracing

300 nl of AAVs (AAV-CBh>EGFP: WPRE, AAV8(VB900088-2238xse)-C, VectorBuilder; AAV-1-hSyn1-dlox-EGFP(rev)-dlox-WPRE-hGHp(A), Virus Vector Facility-VVF115; AAV-8-hEF1α-dlox-dTomato-EGFP(rev)-dlox-WPRE-hGHp(A), VVF198; AAV-1-hSyn1-chI-loxP-mRuby3-loxP-SV40p(A), VVF160) were bilaterally injected using the R-480 Nanoliter Microinjection Pump (RWD) at a speed of 100 nl/min using glass pipettes into the ADn (-0.8 AP, 0.75 ML, 2.8 dorsoventral (DV) from brain surface). For retrograde labeling of ADn cells: C57BL6j mice were injected with ∼200-400 nl of rAAV (RetroAAV-hSyn-EGFP, Addgene: 50465) at the following coordinates: -4.5 AP 2.75 ML 3.8 DV. C1QL2-IRES-Cre mice were injected with ∼400 nl of rAAV (RetroAAV-Ef1a-DIO-EYFP, Addgene: 27056) at the following coordinates: -3 AP 0.3 ML 1.3 DV. The pipette was left in place for a few minutes following injection. Following recovery, mice were housed for >1 week (AAV injections) until transcardial perfusion.

In vivo recordings and juxtacellular labeling

Glass electrode recordings in head-fixed mice were performed as previously described[27] (Figure 1). Mice were head-restrained via a custom-made stainless-steel block secured to a heavy-duty frame. The apparatus was mounted to a turntable consisting of a circular aluminum breadboard enabling 360° passive rotation. Head-restrained mice could spontaneously run and rest on a 25-cm diameter plastic running disc covered with thick tissue paper (the distance between the center of running disc and the mouse's head was fixed at ∼7 cm). An inertial measurement unit (IMU, SparkFun OpenLog Artemis, preprogrammed to automatically log data from Global Navigation Satellite System navigation data) was attached to the turntable to enable monitoring of HD information at 10 Hz. A rotary encoder (HEDM-5500#B13, Avago Technologies) was attached to the running disc to monitor the animal's running speed.

Please cite this article in press as: Hijazi et al., Diversity and sensorimotor specialization of head direction cells in the mouse thalamus, Current Biology (2026), https://doi.org/10.1016/j.cub.2026.05.026

The main glass electrode (filled with 3% neurobiotin in 0.5 M NaCl) was lowered towards the ADn. Another glass electrode was lowered to the CA1 pyramidal cell layer of the hippocampus. The experimenter manually rotated the setup to control the animal's heading (average rotation speed: 0.67 degree/s; Table S1) while dynamically adjusting the depth of the main glass electrode between 2 mm and 3.5 mm DV, in order to increase the chances of passing through the receptive fields of HD cells. The experimenter learned to recognize the specific sound (pitch, frequency, temporal pattern) of ADn HD cell spikes via a loudspeaker, along with the abrupt firing rate increase associated with entering a receptive field. Therefore, our dataset is biased towards HD cells versus non-HD cells in the ADn. Once an HD cell was detected, at least one full slow turn was conducted. If no HD cells were detected, the glass electrode was removed from the brain and inserted at a slightly different ML/AP position. This was conducted for both hemispheres during 2-4 h recording sessions over 1-4 days.

Juxtacellular labeling was performed after completing recordings from all detected HD cells in a recording session. Neurobiotin was delivered via the glass electrode to a recorded cell of interest at the end of the recording session using 200 ms current pulses followed by a 4–7 h recovery period prior to perfusion. In a subset of experiments (n=2 mice), acute silicon probe recordings were conducted following glass electrode recordings and localization of the ADn, as previously described.[27]

Sensory stimuli

After detecting HD cells with stable recordings while the mouse was passively rotated, sensory stimuli were presented when the mouse was facing the PFD or was outside the PFD. The recording room was kept in photopic conditions (600-700 lux) when stimulation was delivered. A customized LED strip (7 cm long) was attached to the setup facing the mouse's head, 10.5 cm away from the animal, providing a viewing angle of approximate ~30 degrees on each side from the centre of the LED strip (egocentric cue). The light stimulus consisted of light-ON (maximum luminance: 2,000–2,400 lux) and light-OFF (minimum luminance, i.e., room luminance), alternatingly presented for different durations (200 ms–10 s) and trials (9–138 trials) per cell. This stimulus was used to assess transient or sustained responses. The 'click' sounds (broad frequency; intensity at mouse ear position: 45–73 dB; average duration 10 ms) were either actual finger clicks or were recordings of a finger click played through a loudspeaker (fixed distance of 120 cm from the mouse; allocentric cue). The timing of light-ON/OFF for LED and sound stimuli were manually controlled with a customized module. To deliver the LED or sound stimuli, the mouse was positioned within and/or outside the PFD of the cell in a randomized order.

Slice physiology

Whole-cell recordings of cells within ADn were performed as following: after decapitation, brains were placed in an ice-cold partial sucrose-based solution containing (in mM): sucrose 70, NaCl 70, $NaHCO_3$ 25, KCl 2.5, NaH_2PO_4 1.25, $CaCl_2$ 1, $MgSO_4$ 5, sodium ascorbate 1, sodium pyruvate 3, and D(+)-glucose 25 (carboxygenated with 5% CO_2/95% O_2; 305 mOsmol/kg). Coronal slices from the ADn (250 μm thick) were obtained with a vibrating slicer (Leica VT1200s). Next, the slices recovered at room temperature for 1 h incubated in holding artificial cerebrospinal fluid (ACSF) containing (in mM): 127 NaCl, 25 $NaHCO_3$, 25 D(+)-glucose, 2.5 KCl, 1.25 NaH_2PO_4, 2 $CaCl_2$, 3 sodium pyruvate, 1 sodium ascorbate, and 2 MgCl2 (carboxygenated with 5% CO_2/95% O_2; 310 mOsmol/kg). Slices were then transferred into the recording chamber where they were continuously perfused with recording ACSF (in mM): 127 NaCl, 25 $NaHCO_3$, 25 D-glucose, 2.5 KCl, 1.25 NaH2PO4, 1 MgCl2, and 2 CaCl2 (310 mOsmol/kg). Cells were visualized using an upright microscope (BX51WI, Olympus) equipped with oblique illumination optics (WI-OBCD; numerical aperture 0.8) and a 40× water-immersion objective. Images were collected by a CCD camera (Oxford Instruments Andor Lt) operated by ImageJ software. ADn cells were identified by their location and typical rebound-burst following a hyperpolarizing current. Electrophysiological recordings were acquired using HEKA EPC10 (10 Hz sampling rate) at 32°C with HEKA PATCHMASTER for data acquisition. Patch pipettes were pulled from borosilicate glass (Warner instruments) with an open tip of 3.5–5 MegaOhm of resistance and filled with intracellular solution containing (in mM) 125 K-gluconate, 10 NaCl, 2 Mg-ATP, 0.2 EGTA, 0.3 Na-GTP, 10 HEPES and 10 K2-phosphocreatine, pH 7.4, adjusted with KOH (280 mOsmol/kg), with 5 mg/mL biocytin (Sigma-Aldrich) to fill the cells. Series resistance was kept under 20 MΩ with bridge balance and capacitance fully compensated (using PatchMaster software); cells that exceeded this value were not included in the study. Cells were filled with biocytin for at least 10 min.

Intrinsic passive and active membrane properties were recorded in current-clamp mode at resting membrane potential by injecting 500-ms of increasing current stimuli from -250 pA to +500 pA, at intervals of 50 pA. Data analysis was conducted using a custom-designed script in Igor Pro-9.0 (Wavemetrics).

Following the recordings, slices were fixed for 2 hours with 4% paraformaldehyde (PFA) and stored in 0.1 M phosphate buffer (PB; pH 7.4) at 4°C.

Histology

For tissue processing, procedures were performed as previously described.[65,66]

Transcranial perfusion and sectioning

Mice were deeply anesthetized with sodium pentobarbital (50 mg/kg i.p.) and transcardially perfused with saline followed by a fixative solution containing 4% PFA (w/v, Sigma-Aldrich), 15% saturated picric acid (v/v, Sigma-Aldrich), and 0.05 % glutaraldehyde (w/v, distilled grade, TAAB Laboratories Equipment Ltd) 0.1 M PB. Some brains were post-fixed overnight in fixative lacking glutaraldehyde. After washing out the fixative, brains were stored in 0.1 M PB with 0.05% sodium azide at 4°C. Brains were sectioned at

Please cite this article in press as: Hijazi et al., Diversity and sensorimotor specialization of head direction cells in the mouse thalamus, Current Biology (2026), https://doi.org/10.1016/j.cub.2026.05.026

70 μm thickness using a vibrating microtome (VT 1000S vibratome, Leica Microsystems) and stored in 0.1 M PB with 0.05% sodium azide at 4°C.

For the visualization of neurobiotin-labeled processes with fluorescence microscopy, brain sections were permeabilized in Tris-buffered saline (0.9% NaCl buffered with 50 mM Tris, pH 7.4; TBS) with 0.3% Triton X-100 (TBS-Tx) or via rapid 2x freeze–thaw (FT) over liquid nitrogen. Cy3- or Cy5-conjugated streptavidin (Jackson ImmunoResearch) was applied at 1:500 dilution in TBS-Tx (or PB if permeabilized with FT) for 4 h at room temperature (RT) or overnight at 4°C. Sections were washed in TBS-Tx or TBS/PB (if permeabilized with FT) and mounted to glass slides in Vectashield (Vector Laboratories) and sealed with nail varnish. For the FT method, sections were first incubated for 4 hours in 20% (w/v) sucrose in 0.1 M PB. Sections were transferred to a foil plate and were treated with two rounds of rapid freeze and thaw cycles over liquid nitrogen before being returned to the glass vials to be washed three times (each for 10 minutes) in 0.1 M PB.

For immunohistochemical tests, sections were initially blocked in TBS/TBS-Tx with 20% normal horse serum (NHS, Vector Laboratories) in TBS/TBS-Tx for 1 h. This was followed by incubating with primary antibodies with 1% NHS in TBS/TBS-Tx for 2-5 days at 4°C (see key resources table for list of primary antibodies). Control sections were included that lacked the primary antibodies. Subsequently, sections were washed 3 times in TBS/TBS-Tx, then incubated with secondary antibodies in 1% NHS in TBS/TBS-Tx for 4 h RT or overnight at 4°C. The following secondary antibodies (and dilutions) were used in various combinations (all raised in donkey): anti-mouse Alexa Fluor 405 (1:250) from Invitrogen, anti-guinea pig DyLight 405 (706-475-148) (1:250), anti-guinea pig, anti-rabbit, and anti-mouse Alexa Fluor 647 (706-475-148, 711-605-152, 705-605-151) (1:500) from Jackson ImmunoResearch, and goat anti-rabbit Alexa Fluor 405 (1:250) from Invitrogen. After 3 washes (10 minutes per wash) in 0.1 M PB, sections were mounted to glass slides in Vectashield and sealed with nail varnish.

For diaminobenzidine (DAB)-based horseradish peroxidase (HRP) reactions to visualize neurobiotin-labeled processes with light microscopy, some sections were blocked for 10 min at RT in 1% hydrogen peroxide (H_2O_2) in 0.1 M PB. Next, sections were incubated overnight at 4°C in 1:100 biotinylated goat anti-rabbit IgG (BA-1000, Vector Laboratories) in TBS containing 1% NGS. After washing 3 times in TBS, sections were incubated for 3 days at 4°C in avidin-biotinylated HRP complex (Vectastain ABC Elite kit, Vector Laboratories) in TBS. Subsequently, peroxidase was visualized using a mix of 1% nickel ammonium sulphate, 0.4% ammonium-chloride, and 3,3-DAB (0.5 mg/ml, Sigma-Aldrich) developed with 0.01% H_2O_2. After washing in PB, sections were treated with 0.25% osmium tetroxide (OsO_4, TAAB Laboratories Equipment Ltd, UK) in 0.1 M PB for 5 min. Next, after washing in 0.1 M PB at least four times, sections were transferred onto slides in chrome alum gelatin and dried in air. Sections were then incubated in fresh xylene for 10 min before being quickly mounted in DePeX mounting medium.

Microscopy

For documentation (tiles or z- stacks) and qualitative evaluation for brain regions of interest, an AXIO Observer Z1 microscope (LSM 710; Zeiss) equipped with Plan-Apochromat objectives (magnification/numerical aperture: 10×/0.3, 20×/0.8 and 40×/1.4) was used to acquire images (Axiovision or ZEN Blue 2.6 software) across different fluorescence channels. For confocal microscopy, DIC M27 Plan-Apochromat 20×/0.8, 40×/1.4, 63×/1.4 and alpha Plan-Apochromat 100×/1.46 objectives were used. The following channel specifications were used for the detection of Alexa405, Alexa488/EYFP, Cy3, and Cy5: 405 nm: 405-30 solid-state laser, attenuation filter ND04, MBS-405, emission spectral filter 409–499 nm; 488 nm: Argon laser, MBS-488, emission spectral filter 493–542 nm; 543 nm: HeNe laser, MBS-458/543, emission spectral filter 552–639 nm; 633 nm: HeNe laser, MBS-488/543/633, emission spectral filter 637–757 nm. The pinhole was set to ~1 Airy Unit for each channel to maintain a consistent optical slice thickness (0.6-0.7 μm) across all channels. Channels were acquired sequentially with beamsplitters set to minimize spectral overlap between channels (ZEN Black 14.0 software).

Neurons were traced using a drawing tube attached to a light microscope (Leitz Dialux22, Leica). After alignment of the tracings of consecutive sections, drawings were overlaid and copied onto a single sheet of tracing paper then digitized.

Quantification of ADn cells

ADn cells were imaged using tiled z-stacks of the full ADn, with a step size of 1 μm, using a 40×/1.3 NA (oil immersion) objective. Colocalization of GFP+ cells, CR+ cells, C1ql2+ cells and DAPI was quantified using the Cell Counter plugin in ImageJ based on 2-5 sections per mouse from n=2-3 mice. The proportion of CR+ cells or C1ql2+ cells was calculated by dividing the number of CR+ cells or C1ql2+ cells by the total number of DAPI+ nuclei. Small glial cell nuclei were excluded using a size threshold.

Analysis of electrophysiological data

Head direction classification

By visualizing labeled cells, we confirmed that recorded but unlabeled cells from either the same penetration site or from closely aligned coordinates were located in the ADn (Figures 1D and S1). Spikes were isolated by thresholding high-pass filtered voltage traces of their peaks and validated by using principal component analysis and/or visual inspection in Spike2 software (Cambridge Electronic Design, Cambridge, UK). In total, we recorded 143 ADn cells. We analyzed recordings that were longer than 100 s and with clear spikes isolated. A total of 26 cells were excluded because of lacking full coverage of 360° angles, and 21 cells were excluded due to unavailable IMU data or unclear spikes. Rotation speed (angular head velocity) was computed as the wrapped difference between consecutive head-direction samples and presented in degrees per second (deg/s). Periods in which rotation speed was below 0.1 deg/s were excluded to remove stationary intervals.[21]

The directional tuning curve for each cell was obtained by plotting the firing rate as a function of the mouse's directional heading, divided into bins of 6°. The firing rate was computed based on the total number of spikes divided by the total time in that bin. All HD properties-related parameters were analyzed based on published parameters[67] using custom Python scripts. The mean vector length (Rayleigh's *r*), a measure of the non-uniformity (or directionality) of the directional tuning curve, was calculated from time-normalized binned data, and can vary between 0 (a uniform distribution) and 1 (a non-uniform distribution). From the directional tuning curve fitted with von Mises distributions, we computed four parameters (Figure S2A): (1) preferred firing direction (PFD); (2) peak firing rate, the highest firing rate of the directional tuning curve rate, which indicates the firing rate when the mouse is facing in the cell's PFD; (3) directional tuning width, the range of head directions over which the cell fires; and 4) background firing rate, the average firing rate when the mouse is facing outside of the directional firing range of the cell. All polar plots are based on tuning curves smoothed with a Gaussian function[68] to avoid deviations caused by small fluctuations in the raw directional tuning curve.

Based on published criteria and subjective assessment of the directional tuning curve, we defined an HD by the following criteria: (1) $r > 0.30$; (2) 95th percentile of its corresponding null distribution (3) probability of a non-uniform distribution (Rayleigh test) of $p < 0.001$. For the shuffling procedure, the entire sequence of spikes was randomly time-shifted and the corresponding mean vector length was calculated (the procedure was reiterated 1,000 times for each permutation).

Other parameters analyzed include (1) Directional coherence. Directional coherence is a measure of the smoothness in the firing rate versus HD tuning curve. The firing rate for each directional bin is correlated to the firing rates in the two immediately adjacent neighboring bins (CW and CCW directions) and an overall correlation is calculated across all bins. This measure would be high for cells that have a strong, continuous, and smooth looking tuning curve and low for cells that have a jagged, irregular, and uneven looking tuning curve. (2) Directional information content. Directional information content is a measure of how many bits of HD information is conveyed by each spike and was calculated by the following formula: directional information content = p_i (l_i/l) log2 (l_i/l), where p_i is the probability that the head pointed in the i_{th} directional bin, l_i is the mean firing rate for bin i, and l is the mean firing rate across all directional bins. (3) Burst index. To measure the extent of burst spiking by HD cells, a burst index score was calculated for each cell. ISI histograms (0–100 ms) from the spike timestamped data for each cell were first computed. Next, a burst index score was computed by counting the number of ISIs that were <30 ms, but >2 ms due to the refractory period, and then dividing this value by the total number of ISIs that occurred between 0 and 100 ms. For this calculation only spikes that occurred when the animal's head was within ±30° of the cell's PFD (60° range) were included. Thus, an HD cell that discharges in bursts would have a burst index measure closer to 1. (4) Coefficient of variation. CV is used to investigate whether there were differences in the regularity of spiking across HD cells from each brain area. CV is calculated by dividing the standard deviation of all the ISIs by the mean ISI.

Burst analysis

Burst analysis was performed using a script in Spike2 (https://ced.co.uk/downloads/scriptspkanal). For each HD cell, spikes were extracted from time periods where the mouse was resting and facing the PFD. The minimum duration of the recording was 20 s, and the minimum detected bursts were set to 4. Recordings that did not meet these thresholds were excluded. The minimum number of spikes per burst was set to 3. The maximum interval between two spikes that signifies the start of a burst was set to 50 ms. The longest interval between two spikes (ISIs) *within* a burst (i.e. intervals longer than this terminate a burst) was set to 30 ms. The following parameters were extracted (Figure S2B): percentage of spikes per burst (number of spikes within bursts/number of all spikes); the mean burst length (average duration of bursts); the inter-spike interval during burst (duration between spikes during a burst); the inter-burst duration (duration between two consecutive bursts); and the mean cycle period (average period between bursts, cycle period = inter-burst duration + burst length).

Responses to stimuli

To investigate responses to light pulses and sound, we analyzed 0.5 s time windows before and after each stimulus using custom scripts in Mathematica (Wolfram Research Inc.). We report the following parameters (Tables S2 and S3): *response frequency*, median firing rate after the stimulus; *significance*, Wilcoxon signed-rank test, comparing the number of spikes before versus after the stimulus (with an alpha value of 0.05); *response magnitude*, the difference between the median firing rates before and after the stimulus; and *response latency*. Response latency was defined by the time at which the firing rate of the cell (bin size, 20 ms) was higher ('excitation') or lower ('inhibition') than the mean firing rate of the pre-stimulus period (0.5 s) ±2.5x the standard deviation of the mean firing rate of the pre-stimulus period (based on Li et al.[69]). If the threshold was below 0 we manually determined the latency. PDFs were computed and plotted in Mathematica from smoothed histograms using Gaussian smoothing method to estimate a continuous distribution of firing rates 0.5 s before and after stimulus. Cells or units with fewer than 6 presented stimuli were excluded. In some cases, we separately analyzed firing patterns within the PFD and outside the PFD (unpreferred firing direction, UPFD). We also analyzed the EMG in relation to sound stimuli using a similar approach.

PCA and cluster analyses

Spike times (0.5 s time windows before and after each stimulus) were binned into 20-ms time windows to compute trial-averaged firing rates for each neuron, yielding a data matrix with time bins as observations and neurons as features. To prevent neurons with higher firing rates from dominating the analysis, firing rates were normalized across time on a per-neuron basis. PCA was performed on the mean-centered, normalized firing rate matrix using customized code in Python. The three leading

Please cite this article in press as: Hijazi et al., Diversity and sensorimotor specialization of head direction cells in the mouse thalamus, Current Biology (2026), https://doi.org/10.1016/j.cub.2026.05.026

principal components were used in subsequent analyses as 64% of the variance could be explained by them. Using k-means clustering, we determined the optimal number of distinct clusters was 3 by both a k-means silhouette analysis (python: kmeans.inertia).

Statistics

All data are represented as mean ± SEM or median [IQR]. Experimental units (e.g. mice, cells) are specified in the text after the n values. Statistical analysis was carried out in GraphPad Prism, Python, IgorPro and Mathematica. The alpha value was set to 0.05. For data that approximated a normal distribution (tested by the Shapiro-Wilk test), unpaired Student's t tests were used to compare two groups with equal variances and unpaired t tests with Welch's correction were used in two groups having different variances, otherwise Mann-Whitney tests were used. For non-normal distribution data, Wilcoxon signed-rank test was used to assess whether the population mean ranks differ. For comparisons of more than two groups we used Analysis of Variance (ANOVA) for parametric data followed by Tukey's *post-hoc* test, and Kruskal-Wallis test for non-parametric data followed by Dunn's test.